Title: Pangenomics facilitated with structural analysis reveals host $NAD^+$ manipulation as a major virulence activity of bacterial effectors

Short title: Bacterial effectors manipulate $NAD^+$

Michelle T Hulin[1], Wenbo Ma[1*]

[1] The Sainsbury Laboratory, Norwich Research Park, NR4 7UH, United Kingdom

[*] Corresponding author: wenbo.ma@tsl.ac.uk

*The author(s) responsible for distribution of materials integral to the findings presented in this article in accordance with the policy described in the Instructions for Authors is: wenbo.ma@tsl.ac.uk*

**Abstract (200 words)**

Nicotinamide adenine dinucleotide ($NAD^+$) has emerged as a major component in both eukaryotic and prokaryotic immune systems. Recent findings that Toll/interleukin-1 receptor (TIR) proteins function as $NAD^+$ hydrolases (NADase) link $NAD^+$ metabolism with immune signaling. In this study, we investigated how manipulation of host $NAD^+$ metabolism can be employed as a virulence strategy by pathogens. Using the pangenome of the model bacterial pathogen *Pseudomonas syringae*, we conducted a structure-based similarity search for type III effectors (T3Es) with potential NADase activity from 35,000 orthogroups. Thirteen T3Es, including five novel ones, were identified to possess domain(s) related to seven $NAD^+$-hydrolyzing enzyme families. Most *P. syringae* strains encode at least one $NAD^+$-manipulating T3Es, and many have multiple. We experimentally confirmed the type III-dependent secretion and virulence activity of a novel T3E, which shows similarity with both TIR and adenosine diphosphate ribose (ADPR) cyclase. Using AI-based structural prediction and *in silico* molecular docking, we found divergence at the $NAD^+$-interacting positions and confirmed the functional importance of these residues in the TIR T3E HopAM1. This study highlights $NAD^+$ manipulation as a key virulence mechanism and provides insights into how pathogens may promote infection through manipulation of host $NAD^+$ metabolism.

## Introduction

The metabolite and redox agent nicotinamide adenine dinucleotide ($NAD^+$) is a universal co-factor and essential redox carrier involved in diverse cellular processes. Recently research on the Toll/Interleukin-1 receptor (TIR) domain proteins has established a central role of $NAD^+$ in immune signaling across the kingdoms. TIR proteins were first identified as a stretch of ~150 conserved amino acids shared between Toll and Interleukin immune receptors in animals (Gay and Keith, 1991). TIR domains often associate with other domains that sense the presence of pathogens. Upon activation, TIR proteins cleave $NAD^+$ through a N-glycosidase activity (Essuman et al., 2017; Ofir et al., 2021; Wan et al., 2019), producing adenosine diphosphate ribose (ADPR) and nicotinamide (NAM). TIR proteins can also have cyclase activity to produce cyclic ADPR (cADPR) or variants of cADPR (v-cADPR), as well as base-exchange activity to produce nicotinic acid adenine dinucleotide (NAAD) (Angeletti et al., 2022). All these enzymatic activities are dependent on a catalytic Glutamic acid (Glu) within the catalytic site (Burdett et al., 2021; Duxbury et al., 2020). The resulting $NAD^+$-derived molecules activate immune signaling and in some cases metabolite depletion leads directly to cell death (Ofir et al., 2021).

In plants, the TIR domain is often associated with intracellular immune receptors that also contain the nucleotide binding/leucine-rich repeat (NLR) domains (Kourelis and van der Hoorn, 2018). The NLR proteins have been evolved to sense pathogen effectors, which are secreted to promote disease. TIR-NLR-triggered immunity is usually dependant on downstream Enhanced Disease Susceptibility 1 (EDS1)-helper NLR pathways (Adlung et al., 2016). Plant TIRs produce various products, including ADPR, NAM and a v-cADPR (Table 1), through $NAD^+$ hydrolysis (Huang et al., 2022; Jia et al., 2022; Ma et al., 2020; Wan et al., 2019). The structure of v-cADPR was recently identified as an isomer of cADPR and renamed 2'-cADPR (Manik et al., 2022). Other TIR generated products pRib-AMP/ADP, ADPR-ATP and diADPR were shown to bind to and activate specific EDS1 heterodimers (Huang et al., 2022; Jia et al., 2022), indicating these small molecules link TIR activation to EDS1-dependant immune signalling. In addition, TIR-only proteins also exhibit 2',3'-cNMP synthase activity *in vitro* and these cyclic nucleotides may also contribute to immunity (Yu et al., 2022).

With the establishment of $NAD^+$ metabolism as a major theme in innate immunity, it is intuitive to speculate that this process is manipulated by pathogens as a virulence strategy. For example, sequestering/degrading small molecule signals to block downstream signaling, or competing for the $NAD^+$ substrate to generate distinct molecules. Indeed, Tad1 produced by bacteriophages binds to a TIR-produced small molecule as a sponge to interfere with bacterial anti-viral defence (Leavitt et al., 2022). Intriguingly, pathogens can also suppress immunity using TIR effectors. BtpA and BtpB produced by the animal pathogen *Brucella abortus* reduce host $NAD^+$ levels to promote infection (Coronas-Serna et al., 2020). The type III effector (T3E) HopAM1 produced by the plant pathogen *Pseudomonas syringae* cleaves $NAD^+$ and produces 3'-cADPR (originally designated v2-cADPR), which differs from the 2'-cADPR produced by characterised plant TIR proteins (Eastman et al., 2022; Manik et al., 2022).

Apart from the TIR proteins, there are additional enzymes that can cleave $NAD^+$ at either the pyrophosphate bond or the N-glycosidic bond by multiple enzymes (Figure 1; Table 1). The NUDIX (nucleoside diphosphate linked to a variable moiety X) pyrophosphatase enzymes (Srouji et al., 2017) and phosphodiesterases (PDEs) cleave pyrophosphate bonds. Pathogen effector proteins harboring the NUDIX domain include the oomycete pathogen *Phytophthora sojae* effector Avr3b, which hydrolyses NADH, ADPR as well as 2',3'-cNMPs (Dong et al., 2011; Yu et al., 2022) and the *Ralstonia solanacearum* T3E RipN, which alters the NAD+/NADH ratio to dampen immune responses (Sun et al., 2019). The PDE superfamily contains diverse groups with various functions, structures and different catalytic mechanisms (Azevedo et al., 2014). An example of PDE effector is SdeA produced by the animal bacterial pathogen *Legionella pneumophila* (Akturk et al., 2018).

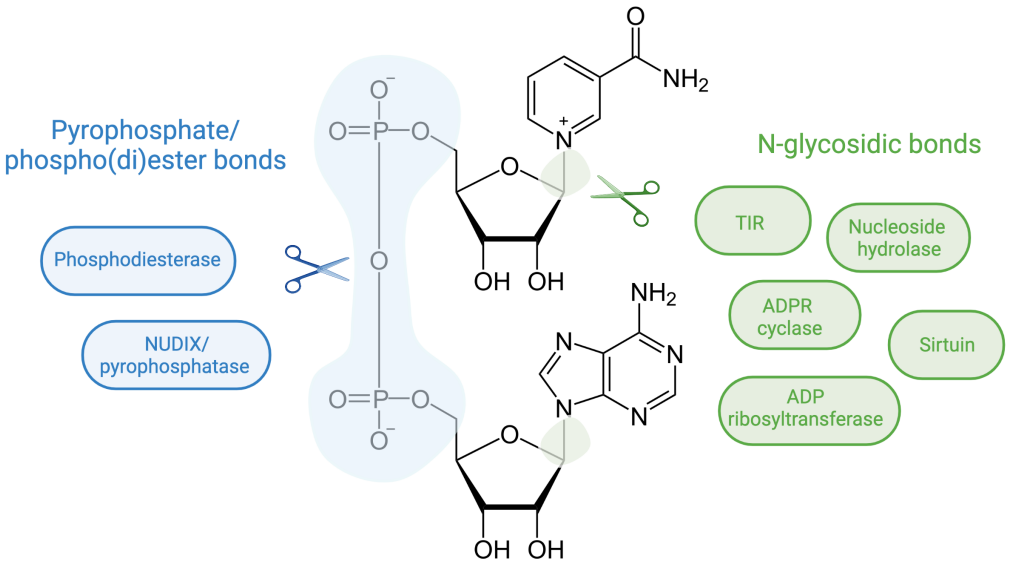


**Figure 1. Enzyme families that may hydrolyse NAD⁺.**
The NUDIX (nucleoside diphosphate linked to a variable moiety X) enzymes and phosphodiesterases (PDEs) cleave the pyrophosphate bond. ADP-ribosyltransferases (ART), nucleoside hydrolases (NH), ADPR cyclases, and sirtuins cleave the N-glycosidic bond.

Enzymes that can potentially cleave the N-glycosidic bond in $NAD^+$ include ADP-ribosyltransferases (ART), nucleoside hydrolases (NH), ADPR cyclases, and sirtuins (Figure 1). ARTs cleave $NAD^+$ to release ADPR for post-translational modifications of proteins and nucleic acids (Corda and Di Girolamo, 2003; Takamura-Enya et al., 2001). However, some ARTs act primarily as $NAD^+$ glycohydrolases and don't require a protein substrate (Ghosh and Caparon, 2006). ART effectors have been identified in various pathogens although most of them are presumed to modify host protein targets (Schreiber et al., 2021). A nucleoside hydrolase effector is the *P. syringae* T3E HopQ1, which was shown to alter purine metabolism (Li et al., 2013) and activate cytokinin signaling by hydrolyzing the cytokinin precursor iP-riboside 5′-monophosphate (iPRMP) (Hann et al., 2014; Li et al., 2013). Sirtuins utilise $NAD^+$ as a co-factor during protein deactylation (Sanders et al., 2010); however, the sirtuin ThsA in *Bacillus cereus* primarily acts to deplete $NAD^+$ during anti-viral immunity (Ofir et al., 2021). Finally, ADPR cyclases have similar activity to TIR proteins to cleave $NAD^+$ into ADPR, cADPR and NAM, despite limited sequence similarity (Lee and Zhao, 2019). So far, pathogen effectors with sirtuin or ADPR cyclase domains have not been identified.

115

116 Here, we employ pangenomic and structure-based similarity searches to identify
117 effectors with potential NADase activity from the model bacterial pathogen *P. syringae*.
118 We found *P. syringae*, as a species complex, has a diverse T3E repertoire with various
119 enzymatic activities that may hydrolyze $NAD^+$, supporting that manipulation of $NAD^+$
120 metabolism is a key virulence mechanism. Furthermore, we examined the structural
121 features of the *P. syringae* TIR proteins using AlphaFold2 and *in silico* docking. This
122 analysis revealed diversity at the $NAD^+$-interacting residues, which may fine tune the
123 enzymatic activities, thus providing insight into how effectors may promote infection
124 through $NAD^+$ manipulation in the host.

125

126 **Results**

127

128 **Pangenome analysis of putative NADases in *P. syringae***

129

130 Traditionally classified into pathovars based on host of isolation, *P. syringae* is a
131 species complex infecting over 180 different plant species (Young, 2010). Utilizing the
132 pangenomic diversity of *P. syringae*, we systematically analyzed NADase-encoding
133 proteins using pipelines illustrated in Figure 2A. *P. syringae* is divided into
134 phylogroups, which broadly correspond to phylogenetic "species" sharing 95%
135 Average Nucleotide Identity (ANI) (Gomila et al., 2017). The major plant pathogens
136 belong to the "primary" phylogroups I, II, III, IV, V, VI and X, which form a monophyletic
137 clade and rely on a canonical *hrp* type III secretion system (T3S) to cause disease.
138 The "secondary" phylogroups VII, IX, XI and XIII include environment-associated
139 strains which may not possess the *hrp* T3S and encode very few T3Es, consistent with
140 their mostly non-pathogenic lifestyle (Dillon et al., 2019; Xin et al., 2018). To examine
141 NADases across the species complex, an initial 2,437 genomes were obtained. After
142 removing lower quality and almost identical genomes, 531 genomes were used in the
143 final analysis. A phylogeny based on the core genome (Figure 2B) shows that these
144 strains represent previously defined phylogroups and additional undefined clades. The
145 genomes were grouped into ≥ 95% identical ANI groups which loosely correspond to
146 defined phylogroups (Supplemental Figure S1). The primary phylogroups grouped at
147 ≥ 85% ANI (highlighted in red on Figure 2B). The secondary phylogroups and other

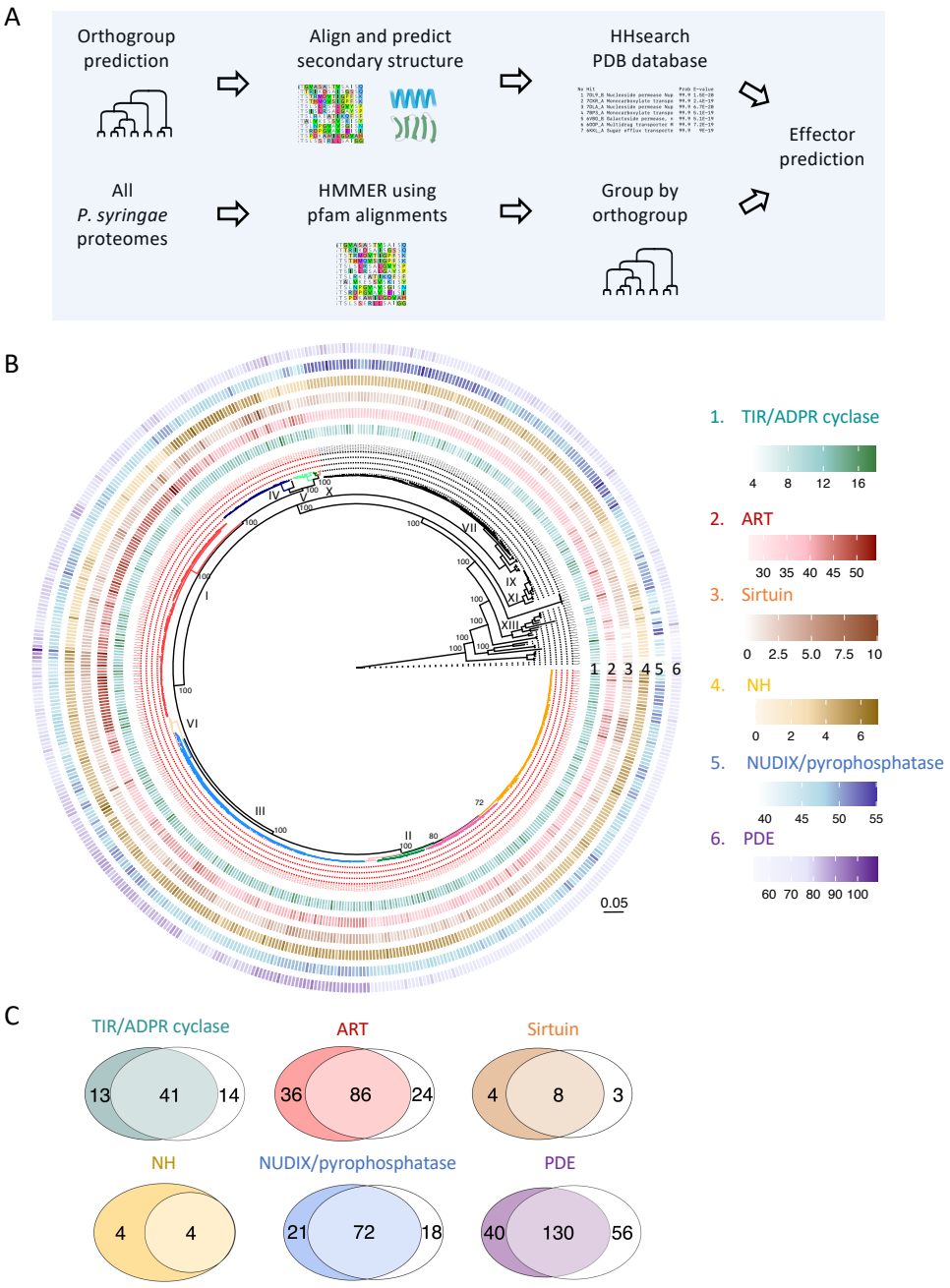


**Figure 2. Identification of NADases encoded in the *P. syringae* species complex.**

A) Two approaches based on HMMER and HHsearch respectively were used to predict all seven NAD hydrolyzing enzyme families from the pangenome of *P. syringae*.

B) NADase genes predicted across the *P. syringae* species complex are mapped onto the maximum-likelihood core genome phylogeny. Numbers of predicted genes from each enzyme family is presented by heatmaps. The phylogeny was generated based on 409 concatenated single copy core genes. The scale shows amino acid substitutions per site. Strains in the primary phylogroups are coloured in red. Due to similarity in enzymatic activity, NUDIX and pyrophosphatase were grouped together, as well as TIR and ADPR cyclase.

C) Venn diagrams to show the number of primary phylogroup specific NADase encoding orthogroups (left), orthogroups shared between primary and secondary phylogroups (middle), and orthogroups specific to secondary phylogroups (right).

genomes labelled as "*P. syringae*" were grouped outside the primary phylogroups at 80% ANI. Two divergent *P. viridiflava* strains, sharing 79% ANI with the rest of the

151 complex, were used as an out-group to root the tree. Orthology analysis defined the
152 pangenome of 2,867,287 protein-encoding genes into 23,583 orthogroups (OGs), with
153 an additional 11,608 singletons. In total, 35,191 OGs were further analyzed to identify
154 candidate NADases.
155
156 Two complementary approaches (HMMER and HHsearch) were employed to identify
157 proteins possessing any of the seven enzymatic domains including ART, NUDIX,
158 pyrophosphatase, PDE, TIR, sirtuin, ADPR cyclase, and nucleoside hydrolase (Figure
159 2A; Supplemental Table S1). Using HMMER-based approach, 146 candidate OGs
160 were identified, whilst the HHsearch-based approach picked up 564 candidates,
161 including 136 being identified by both approaches (Table 2, full details in Supplemental
162 Table S2). Among the 136 candidates are known housekeeping nucleosidases, such
163 as the NUDIX enzyme NudC (OG1452), the Sirtuin CobB3 (OG752), the purine
164 nucleosidase RihA (OG2649), and cyclic-AMP phosphodiesterase CpdA (OG3903)
165 (Drabinska et al., 2020; Fuchs et al., 2010; Gallego-Jara et al., 2021; Petersen and
166 Moller, 2001). In addition, both searches identified the TIR T3E HopAM1 (OG6638)
167 (Eastman et al., 2022) and the ART T3E HopU1 (OG9885) (Fu et al., 2007). The large
168 number of hits (428) uniquely identified from HHsearch indicates this method allowed
169 the detection of divergent homologues. By using both approaches, we maximized the
170 chance of capturing all potential candidates.
171
172 The 574 candidate OGs with potential NADase activity are distributed across the *P.*
173 *syringae* species complex (Figure 2B). On average, each *P. syringae* genome
174 contains 187 NADase-encoding genes, including 131 in core orthogroups (present in
175 ≥ 95% of genomes) and 56 in accessory orthogroups. The distribution of orthogroups
176 into core and accessory genomes varied for each enzyme group (Table 2). For
177 example, 34% of NUDIX/pyrophosphastase orthogroups are in the core genome,
178 whilst only 8% of TIR orthogroups are in the core genome. We next determined the
179 candidate NADase orthogroups specific to the primary phylogroups, which are
180 pathogens that rely on the *hrp* T3S for pathogenesis (Figure 2C; full data in
181 Supplemental Table S2). The majority of candidates are encoded in the genomes of
182 both groups, indicating that they are not directly related to pathogenesis. However, in
183 each enzyme family, there are orthogroups only encoded by the primary phylogroups,

184 suggesting that they may function as virulence factors or facilitate pathogen adaptation
185 to host environment.
186
187 **NADases as Type III effectors**
188
189 To identify T3Es from the NADase candidates, we established a pipeline, which
190 included an initial screen using the program EffectiveT3 (Eichinger et al., 2016)
191 followed by a promoter search for putative *hrp* boxes using FIMO (Grant et al., 2011).
192 Potential novel T3E candidates were further examined for the N-terminal amino acid
193 sequences for secretion signal characteristics (Guttman et al., 2002). The outcome of
194 this analysis revealed 13 OGs as high confidence effector candidates (Table 3;
195 Supplemental Figure S2; A full list before filtering is in Supplemental Table S3). The
196 robustness of this analysis is verified by the successful identification of all the known
197 T3Es with putative NADase-encoding domains: the ART effectors HopF/HopBB,
198 HopO1, AvrRpm, HopS, and HopU1, the NUDIX effector HopAG1, the NH effector
199 HopQ1, and the TIR effector HopAM1. The detection of multiple non-overlapping hits
200 to different enzymes in the same protein also revealed HopAG1 as a multi-domain
201 effector that contains an ART domain in addition to the previously known NUDIX
202 domain. Importantly, we identified five novel NADase T3E candidates, including two
203 ARTs (OG5256, OG18195), one PDE (OG4578), and two TIR/ADPR cyclases
204 (OG8567, OG18056).
205
206 The distribution of known NADase T3Es and novel candidates was mapped on the
207 core genome phylogeny (Figure 3A). 93% of the primary phylogroup strains have at
208 least one NADase T3Es and 72% possess T3Es belonging to more than one enzyme
209 family. On average, each primary phylogroup strain encodes three T3Es that
210 potentially hydrolyze $NAD^+$. Interestingly, three enzymatic activities that are each
211 represented by only one T3E are prevalent in primary phylogroup strains: the NUDIX
212 effector gene *hopAG1* is present in 55% of primary phylogroup strains across nine
213 phylogroups; the NH effector *hopQ1* is found in 31% of primary phylogroup strains
214 across five phylogroups; and the new PDE effector candidate OG4578 is found in 26%
215 of primary phylogroup strains, although restricted to phylogroup II and X. These results
216 indicate $NAD^+$ hydrolysis is a key virulence strategy widely used by *P. syringae*.
217

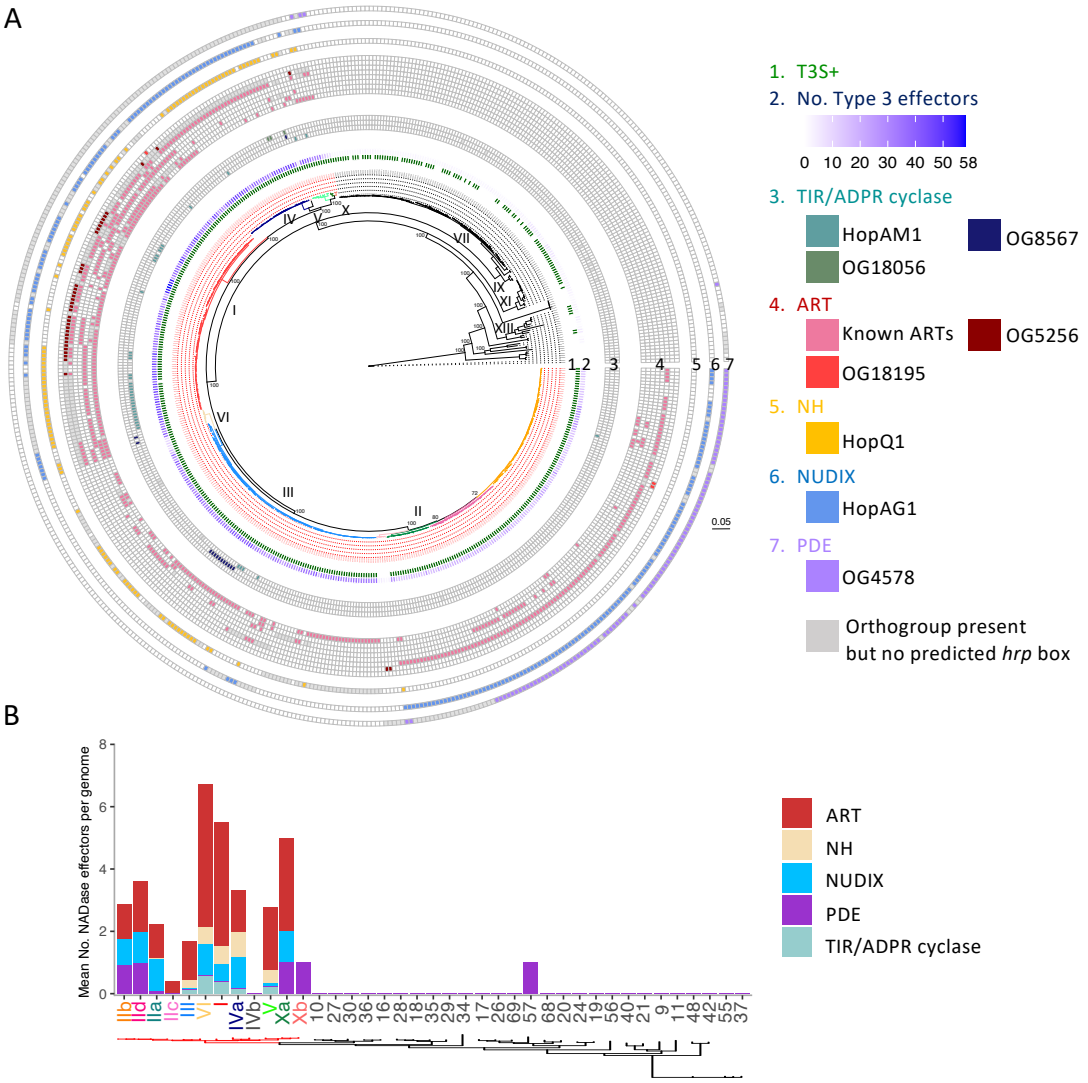


**Figure 3. Predicted NADases as type III effectors in *P. syringae*.**

A) NADase T3Es predicted across the *P. syringae* species complex are mapped onto the maximum-likelihood core genome phylogeny. Strains in the primary phylogroups are coloured in red. The presence of a canonical *hrp* T3SS is presented as Ring 1 (in green) and the number of known T3E genes encoded in each strain is presented in Ring 2 as a heatmap coloured in a scale of white to blue. Ring 3-7 each represents one of the five NADase enzyme families. Known T3Es with putative ART domains are in order: HopF/BB, HopO1, AvrRpm, HopS, HopU1, HopAG1. Presence of each orthogroup is coloured as in the scale, with grey squares indicating the orthogroup is present but with no *hrp* box in the promoter.

B) Mean number of NADase T3Es per phylogroup. The primary phylogroups are labelled with roman numerals, whilst secondary phylogroups correspond to their species number predicted by Average Nucleotide Identity in Supplemental Figure S1. A collapsed version of the core genome phylogeny, with the primary phylogroup clade in red is included for reference.

To better understand the diversity and distribution of NADase effectors in *P. syringae*, we summarize the average number of each enzyme group per genome in each phylogroup (Figure 3B; full details in Table 4). A clear difference between the primary and secondary phylogroups can be visualized, with a significantly larger number of NADase T3Es in the primary phylogroups. The number of ART effectors per genome were particularly high in phylogroups I, VI, IVa, V and Xa. This could at least in part be

225 due to expansion of the HopO and HopF/HopBB families that has been observed
226 previously (Lo et al., 2017). A closer look at the copy number variation of each ART
227 effector across the phylogroups (Supplemental Figure S3) shows that strains within
228 phylogroups III, I and V possess up to four HopF/HopBB family members, whilst HopO
229 is specifically expanded in phylogroup I strains. An increase in copy number was also
230 noted for the TIR effector HopAM1 which is present as two copies in 22% of the
231 genomes that encode it. This observation indicates the effectors may impact host
232 processes in a dose-dependent manner.
233
234 In summary, this analysis demonstrate that the *P. syringae* species complex has
235 evolved effectors that contain diverse NADase domains, which potentially manipulate
236 levels of $NAD^+$ in the plant hosts. Many strains possess a variety of enzyme groups
237 with multiple gene copies, consistent with an important contribution to virulence.
238
239 **Novel NADases T3E candidates**
240
241 ART is the largest NADase T3E family with eight members (six known and two novel).
242 Of the novel candidates, OG18195 is present in only three genomes in phylogroups I
243 and II, whilst OG5256 is present in 139 genomes. Structurally, OG5256 is most similar
244 to the T3E HopU1 (3U0J). Interestingly, *OG5256* gene was found to be downstream
245 of a T3E gene cluster harbouring *hopAG1*, *hopAH1* and *hopAI1* (Supplemental Figure
246 S2). The presence of these upstream effectors in a putative operon may explain why
247 only 37 of the 139 strains had a predicted *hrp* box in the immediate upstream of this
248 gene.
249
250 The candidate PDE effector OG4578 was identified as a protein with homology to
251 FimX EAL phosphodiesterase. FimX was reported to regulate twitching motility in
252 *Pseudomonas aeruginosa* (Kazmierczak et al., 2006), which is unlikely to be a T3E.
253 This OG was present in 238 primary phylogroup strains but only 100 had a predicted
254 *hrp* box promoter. These 100 strains are from a particular clade (Supplemental Figure
255 S4), indicating that OG4578 might be re-purposed to directly contribute to
256 pathogenesis.
257

258 Considering the recent breakthroughs in the functionality of TIR-NLR signalling, we
259 conducted in-depth analysis on the TIR/ADPR cyclase T3E candidates. HopAM1 was
260 the only known TIR T3E from previous studies. Our analysis identified two candidate
261 T3Es: OG8567 as a TIR candidate and OG18056 as an ADPR cyclase candidate.
262 OG8567 is encoded in 22 strains including 15 in the primary phylogroups; only genes
263 in these 15 strains carry *hrp*-box-like promoter sequences. The second candidate
264 OG18056 was predicted as an ADPR cyclase. OG18056 is only present in three *P.*
265 *coronafaciens* pv. *atropurpurea* strains clustered in the primary phylogroup IV which
266 are pathogens of grass species. In the genome assembly GCA_001400695, *OG18056*
267 is within 15 Kb of T3E homologues *hopV1 and hopAA1* and a coronatine biosynthesis
268 operon (Supplemental Figures S2 and S5). In addition, this gene is flanked by
269 transposase genes and conjugation-machinery (*virB* homologues), indicating that it is
270 located in a mobile region of the genome and therefore may have been acquired via
271 horizontal gene transfer.
272
273 Using AlphaFold2 (Mirdita et al., 2022), we generated structure models for HopAM1,
274 OG8567, and OG18056 (Supplemental Figure S6A). The structures were aligned to
275 the TIR domain of the well-characterised human NADase SARM1, with Root-Mean-
276 Square Deviation (RMSD) values of 2.58, 2.78, and 3.01 Å, respectively
277 (Supplemental Figure S6B). A glutamate (Glu) in the position 642 aa in hSARM1 is
278 crucial for its NADase activity (Essuman et al., 2017). Structural alignments confirmed
279 that HopAM1 has a catalytic Glu (E191), as shown previously (Eastman et al., 2022).
280 Similarly, OG18056 also has a Glu (E305) at the corresponding position to hSARM1-
281 642, indicating that it could be an active $NAD^+$-cleaving enzyme. In contrast, the other
282 candidate OG8567 has an isoleucine (I142) at this position; therefore it is less likely to
283 possess NADase activity, or could have a suboptimally positioned catalytic Glu in a
284 nearby position (E139).
285
286 **OG18056 is a novel T3E with structural features similar to both TIR and ADPR**
287 **cyclase**
288
289 The full structural alignment of OG18056 with the hSARM1 TIR domain (Figure 4A)
290 was intriguing because it was identified only from the HHsearch-based analysis, which
291 revealed structural similarity only with ADPR cyclases. Superimposition of OG18056

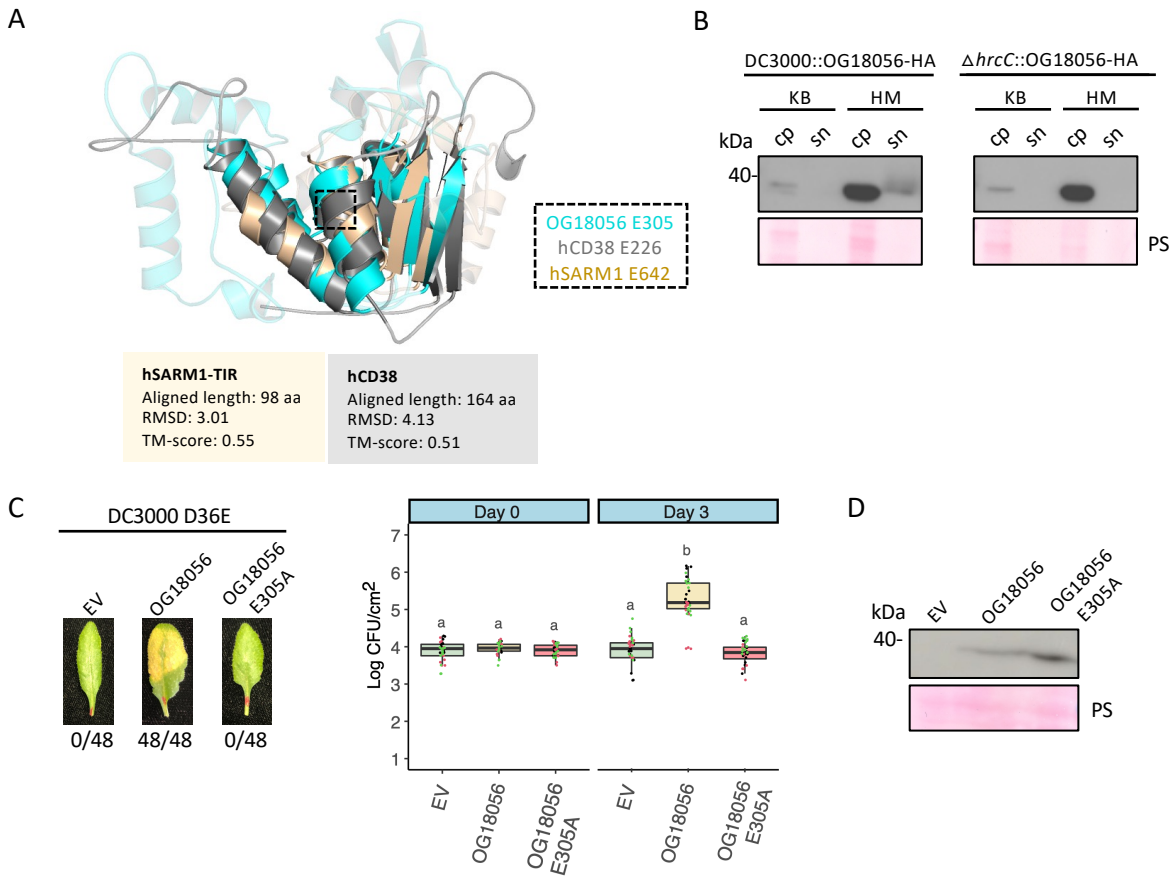


**Figure 4. OG18056 is a novel T3E with similarity to ADPR cyclases.**

A) Alignment of a structural model of OG18056 predicted by AlphaFold2 (in cyan) with human CD38 (6VUA, in grey) and the TIR domain of human SARM1 (6O0R, 561-700 aa, in light brown). Root-Mean-Square Deviation (RMSD) values and TM-scores are presented using OG18056 as the reference. For visualisation purposes, sequences outside the alignment region were removed and those that did not align within the region are more transparent. The predicted catalytic Glu residues are aligned in three structures and highlighted with a box.

B) Immunoblot showing the induction and secretion of OG18056 by *P. syringae*. OG18056-HA was expressed in PstDC3000 or the T3S mutant Δ*hrcC* under its native promoter. The bacteria were cultured in the rich medium Kings B (KB) or a Hrp-inducing minimal medium (HM). Proteins were extracted from cell pellet (cp) or supernatant (sn) and the protein levels of OG18056 were determined by western blotting using an anti-HA antibody. Ponceau S (PS) staining was used as the loading control.

C) OG18056 enhanced the virulence of the effectorless mutant PstDC3000 D36E on *Arabidopsis thaliana*. Upper: disease symptom development by D36E carrying the empty vector, OG18056 or OG18056(E305A). Numbers show the number of leaves with symptoms recorded over three independent experiments. Leaves were inoculated with 5 x $10^6$ CFU/ml inoculum and imaged 3 days later. Lower: population count of the D36E transformants in *A. thaliana*. Boxplots show the day 0 and day 3 populations in Log CFU/$cm^2$. Individual data points with different colors represent results from three separate experiments. Tukey-HSD significance groups extracted from ANOVA are presented.

D) OG18056 and its mutant were expressed under its native promoter in PstDC3000 D36E. Immunoblot showing OG18056 and OG18056(E305A) expression when bacteria were grown in Hrp-inducing minimal medium.

292

293 with the human ADPR cyclase hCD38 showed a RMSD value of 4.13 Å. Although this
294 RMSD value is higher (indicating lower similarity) than that of the hSARM1 alignment
295 (3.01 Å), the alignment length was greater (164 aa) than that aligned to hSARM1 (98
296 aa). In addition, OG18056-E305, which was aligned to the catalytic residue (E642) in
297 hSARM1, could also be aligned to the catalytic residue (E226) of hCD38 (Munshi et

298 al., 2000). Topology analysis indicated that the active sites of all three enzymes have
299 similar arrangement of alternating α helices and β sheets (Supplemental Figure S7).
300 These results suggest OG18056 is structurally similar to both ADPR cyclase and TIR,
301 hence may have a novel NADase activity.
302
303 To experimentally confirm that OG18056 is a T3E, we tested its expression pattern
304 and potential T3S-dependent secretion. The gene encoding OG18056 was expressed
305 in *P. syringae* strain PstDC3000 under its native promoter with a C-terminal HA tag.
306 The bacterial cells were induced in a *hrp*-minimal medium (HM); total and secreted
307 proteins were detected by immunoblotting (Figure 4B). Our results showed that
308 *OG18056* was drastically induced in the minimal medium, an expression pattern
309 commonly observed in T3S-related genes. Furthermore, OG18056 proteins were
310 detected in the supernatant of PstDC3000, but not a T3S mutant Δ*hrcC*, confirming it
311 is a true T3E that can be secreted in a T3S-dependent manner.
312
313 To examine the potential virulence activity of OG18056 when delivered by bacteria
314 during infection, we expressed the gene in the effectorless mutant D36E of
315 PstDC3000. Inoculation of D36E expressing OG18056 ($5 \times 10^6$ cfu/mL) into *A. thaliana*
316 leaves resulted in chlorotic symptoms (Figure 4C). *In planta* bacterial growth (after
317 inoculation at a lower dose, $5 \times 10^5$ cfu/mL) was also significantly increased. Both
318 virulence functions required the predicted catalytic residue E305, indicating that the
319 putative ADPR cyclase/TIR NADase activity is responsible for promoting bacterial
320 infection by this novel T3E. Both OG18056 and the E305A mutant were confirmed to
321 be expressed in D36E in *hrp*-inducing medium (Figure 4D).
322
323 **Characterization of $NAD^+$-binding residues in bacterial TIR proteins**
324
325 Different NADases produce specific products. The previously characterized TIR T3E
326 HopAM1 produces a variant of cADPR (3'-cADPR) that is different from the variant 2'-
327 cADPR produced by plant TIRs (Manik et al., 2022). Over-expression of HopAM1 in
328 *Nicotiana benthamiana* triggers cell death. This activity requires the catalytic residue
329 E191, indicating that the cell death is induced either through the NADase products or
330 $NAD^+$ depletion (Eastman et al., 2022). Interestingly, HopAM1 triggered cell death is

331 independant of EDS1, indicating that it is through a pathway/mechanism distinctive
332 from most plant TIR-NLRs (Choi et al., 2017). Residues in the catalytic pocket of
333 NADases influence the preference of products after $NAD^+$ hydrolysis and can switch
334 enzymatic activity between $NAD^+$ hydrolysis and cyclization (Graeff et al., 2009;
335 Toshchakov and Neuwald, 2020). To gain insight into how this fine tuning of the
336 NADase activity may affect the function of HopAM1, we investigated the structural
337 diversity of the TIR and ADPR cyclase proteins in *P. syringae*.
338
339 Alphafold2 was used to generate 3D structure models for 63 of the 68 OGs predicted
340 from *P. syringae* pangenome using the consensus sequence of each orthogroup (five
341 were too short for structural prediction) (Figure 5A; Supplemental Table S4). 84% of
342 the predictions scored ≥ 70 pLDDT (Predicted Local Distance Difference Test)
343 indicating the prediction had worked well. We used the program P2RANK (Krivak and
344 Hoksza, 2018) to predict if there was a ligand binding pocket in each protein and in
345 parallel, alignments were performed with the TIR domain of hSARM1 to identify the
346 positions of putative catalytic residues. The RMSD scores of the *P. syringae* proteins
347 with hSARM1-TIR ranged from 1.75 to 5.47 Å, confirming structural homology
348 (Supplemental Table S4). 43 proteins were predicted to have pockets at the position
349 aligning to the hSARM1-TIR catalytic site. The structures of these 43 proteins were
350 aligned pairwise using fr-tmalign (Pandit and Skolnick, 2008) and a dendrogram was
351 constructed based on RMSD scores to represent their structural similarity (Figure 5B).
352 The three T3E candidates were scattered across the dendrogram. OG18056 is
353 clustered with other divergent TIR-like proteins outside the clade that showed higher
354 similarity with hSARM1, consistent with our earlier analysis suggesting that OG18056
355 is more similar to ADPR cyclases.
356

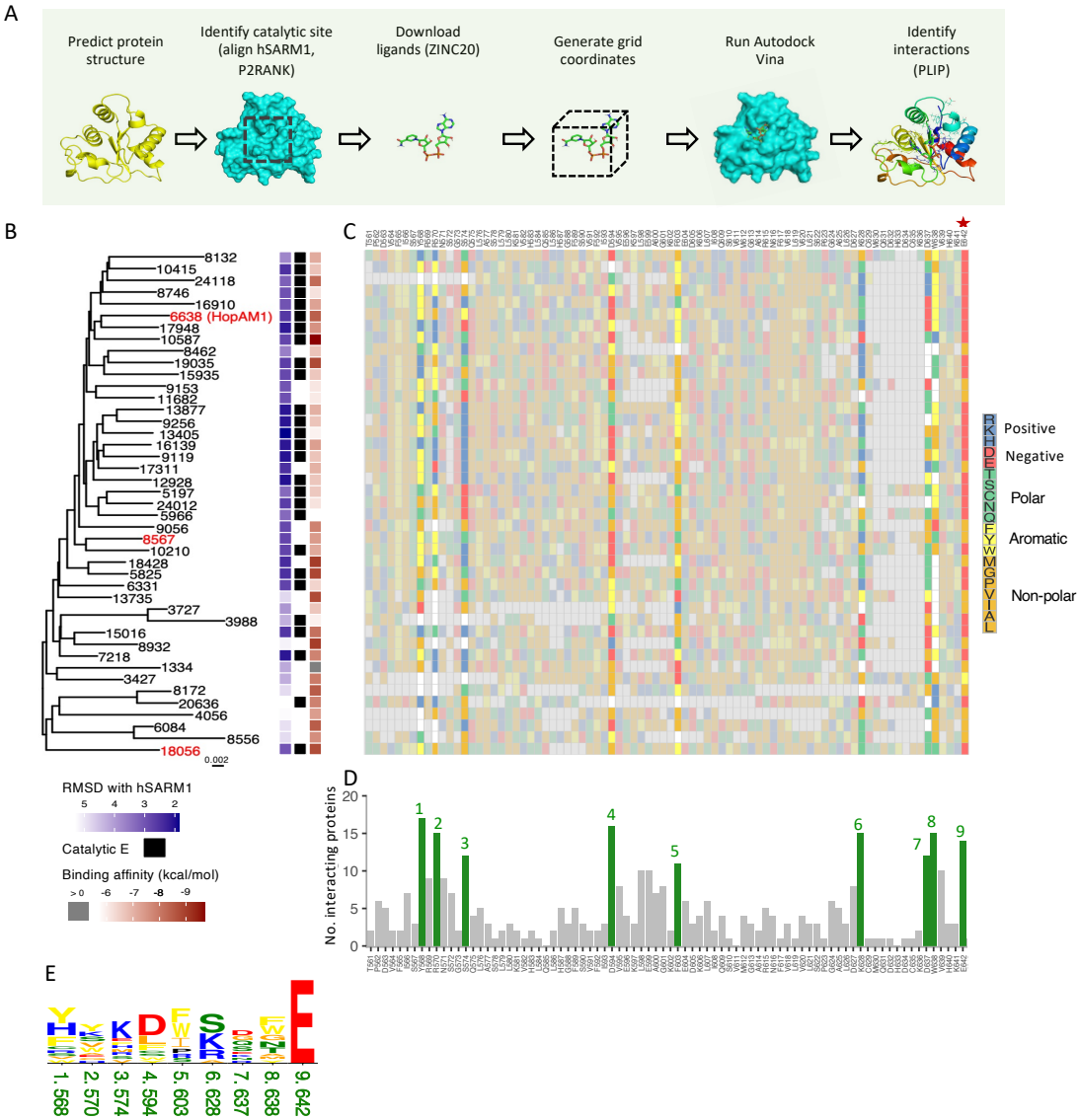


**Figure 5. Structural analysis revealed diversity in the active site of *P. syringae* TIR proteins.**

A) A bioinformatic pipeline used to generate 3D structure models of candidate NADases and predict NAD⁺-binding sites and residues.

B) A dendrogram based on structural similarity of 42 TIR proteins and the one ADPR cyclase homologue (OG18056) predicted from *P. syringae* pangenome. The dendrogram was built by the phylip program fitch using a distance matrix based on RMSD values from pairwise structural alignments. The RMSD values were normalized by alignment length. The three predicted TIR/ADPR cyclase T3Es are highlighted in red. Mapped onto the dendrogram is information regarding the structural alignment for each protein with hSARM1-TIR. The RMSD with hSARM1 is shown with a blue heatmap. A black box indicates that the protein had a glutamate aligning to the catalytic residue E642 in hSARM1-TIR. The NAD⁺ binding affinity of each protein is also presented.

C) Structually equivalent amino acids that aligned to hSARM1-TIR for each *P. syringae* TIR protein. The residues are ordered based on hSARM1-TIR positions and colour-coded by biochemical features. Nine positions that were frequently predicted to bind NAD⁺ during *in silico* docking are highlighted (also see D), whilst other positions are greyed out. The catalytic Glu (E642 in hSARM1-TIR) is labelled with a star.

D) Nine positions were predicted to bind NAD⁺ in more than ten *P. syringae* TIR proteins. These include residues corresponding the hSARM1 catalytic residue E642 (position 9), the nearby residues 628, 637 and 638 (positions 6-8), as well as residues 568, 570, 574, 594 and 603 (positions 1-5), which are further upstream.

E) Sequence logo generated for the nine positions that interacted with NAD⁺ showing frequency of different amino acids in each position. Amino acids are colour-coded as in (C).

359 We next conducted a docking analysis using Autodock Vina to model the binding of
360 $NAD^+$ within the pocket coordinates predicted by P2RANK (Figure 5A). From the eight
361 different models predicted from each structure, the $NAD^+$ binding affinity was
362 calculated using the top model from the prediction (Figure 5B). The results show that
363 most structures, except for one, bind $NAD^+$ with affinities ranging from -5.71 to -9.72
364 kcal/mol (Supplemental Table S4). A monomeric hSARM1 TIR domain (561-700 aa
365 scored -7.20 kcal/mol, indicating the *P. syringae* TIRs had similar predicted binding
366 affinities to a known NADase). In summary, 42 of these proteins may have the potential
367 to bind $NAD^+$ through a TIR-like catalytic pocket and 27 of them have a Glu aligned to
368 the hSARM1-TIR catalytic residue E642, indicating that they may be active NADases.
369
370 We next investigated whether there were particular positions that were important for
371 $NAD^+$ interaction. Using the structural alignment, we pulled out residues at each
372 structurally equivalent position to hSARM1-TIR from each *P. syringae* protein to
373 examine conservation (Figure 5C; Full region is presented in Supplemental Figure S8).
374 In parallel, the program plip (Salentin et al., 2015) was used to predict which residues
375 may interact with $NAD^+$ for each protein. Using hSARM1-TIR domain as a reference,
376 we then calculated the number of proteins that had a residue predicted to interact with
377 $NAD^+$ in each structurally equivalent position (Figure 5D). This analysis revealed nine
378 positions that were predicted to bind $NAD^+$ in more than ten proteins. For clarity we
379 refer to the positions based on the hSARM1 number. These include residues
380 corresponding the hSARM1 catalytic residue 642, as well as nearby residues 628, 637
381 and 638. In addition, clusters of residues further upstream from the catalytic Glu,
382 corresponding to positions 568, 570, 574, 594 and 603 in hSARM1 were also
383 frequently predicted to bind $NAD^+$. The higher frequency of the predicted binding of
384 these residues to $NAD^+$ may indicate their conserved importance in substrate binding.
385 Indeed, some of the equivalent positions have been shown to be required for $NAD^+$-
386 binding and/or NADase activity in ADPR cyclases (Liu et al., 2007) and TIR proteins
387 in plants and bacteria (Essuman et al., 2017; Horsefield et al., 2020; Shi et al., 2022).
388
389 We also analyzed the conservation levels in each of the nine $NAD^+$-binding positions
390 across the *P. syringae* proteins (Supplemental Table S5). Except for the highly
391 conserved catalytic Glu residue (E642 in hSARM1-TIR), a high level of diversity was
392 observed in all other positions (Figure 5E). Nonetheless, some trends appear: 1)

393 aromatic residues (F, W or Y) were common at positions corresponding to hSARM1
394 568, 603 and 638; 2) positively charged residues (K or R) were common at positions
395 574 and 628; 3) position 594 was frequently negatively charged (D). Residues
396 corresponding to positions 568, 574, 594 and 638 were shown to modulate the cyclase
397 activity, substrate preference, and ratio of ADPR/cADPR products generated by the
398 CD38 homologues (Graeff et al., 2009; Ramakrishnan et al., 2010; Tohgo et al., 1997).
399 Therefore, specific residues in these positions may fine tune the enzymatic activity.
400
401 **Functional analysis of the $NAD^+$-binding residues in HopAM1**
402
403 To experimentally examine the functional relevance of the nine $NAD^+$-binding residues
404 and their diversity, we generated mutants of HopAM1 that may alter its activity.
405 Because cADPRs have been shown to predominantly produced by plant TIRs and
406 HopAM1, we were interested in reducing the cyclase activity by changing residues to
407 those in hSARM1 and hCD38, which are greater $NAD^+$ hydrolases, preferentially
408 producing ADPR rather than cADPR. For this purpose, we generated eight mutants
409 with specific substitutions of six positions based on the corresponding residues in
410 either hSARM1 or hCD38. Some mutations were also made based on studies of these
411 positions in previous studies (Table 5). A previous study of hCD38 showed a negative
412 amino acid at position corresponding to hSARM1 594 reduces cyclase activity (Graeff
413 et al., 2009). The residue in HopAM1 is D132 which is already negatively charged, so
414 we didn't generate any mutants of this residue. The catalytic E191A mutant (position
415 642) was included as a control. The positions of these residues in the HopAM1
416 structure docked with $NAD^+$ are presented in Figure 6A. These mutants were
417 expressed in *N. benthamiana* using *Agro*-infiltration (Supplemental Figure S9) and the
418 cell death phenotype was monitored. The mutant alleles were also expressed in the
419 effectorless mutant D36E (introduced on the plasmid pUCP20TK under the native
420 *hopAM1* promoter) and infiltrated into *N. benthamiana* leaves at a concentration of 2
421 x $10^8$ cfu/mL in order to confirm the cell death-triggering activities (Supplemental
422 Figure S10). Similar observations were made from both experiments.
423

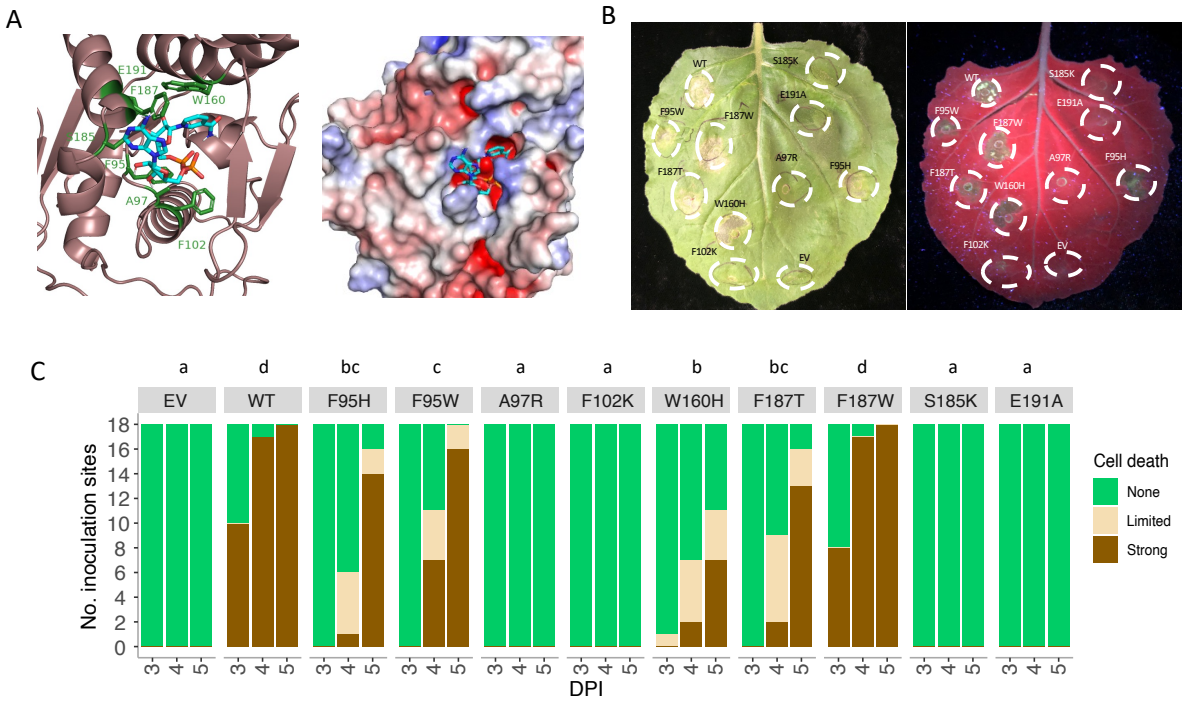


**Figure 6. Characterization of NAD⁺-binding residues for cell death inducing activity of HopAM1.**

A) Predicted structural model of HopAM1 docked with NAD⁺ with residues subjected to mutational analysis highlighted in green. The electrostatic image of the surface of HopAM1 active site is also presented with regions of positive, neutral and negative charge shown in blue, white and red respectively.

B) Cell death induced by HopAM1 and its mutants after transient expression in *N. benthamiana* by *Agro*-infiltration. Representative image of a *N. benthamiana* leaf five days post *Agro*-infiltration (DPI) is presented. The same leaf imaged under ultraviolet light is included to better visualize the cell death lesions. WT: wild-type; EV: empty vector.

C) Quantitative analysis of the cell death phenotype induced by various HopAM1 mutants. The appearance of cell death for each mutant was monitored at 3, 4, and 5 DPI, and scored as either no cell death (in green), weak cell death (limited, patchy appearance, in light brown) and strong cell death covering the whole inoculation site (dark brown). Statistical groupings of an ANOVA comparing cell death scores are shown above the graph. These results are from three independent experiments.

Three of the eight mutants, A97R, F102K, and S185K, showed no visible cell death, similar to the catalytic mutant E191A (Figure 6B; Figure 6C; Supplemental Figure S9). Both hCD38 and hSARM1, having a low cyclase activity, have an R at the corresponding position to A97 (see Table 5). Likewise, both hCD38 and hSARM1 have a K at the corresponding position to F102, and hSARM1 also has a K at the corresponding to S185. Therefore, these mutants could have reduced the cyclase activity of HopAM1, leading to no cell death.

Among the five mutants that were still able to cause cell death after 5 days, four showed slower and weaker phenotype. For residues F95 and F187, we made mutations to two different amino acids (F95 to W or H, and F187 to T or W).

437 Hydrophobic aromatic residues at these positions have been shown to alter the activity
438 and ADPR/cADPR product ratio of CD38 homologues (Graeff et al., 2009;
439 Ramakrishnan et al., 2010). Mutation of F95 to either W or H slowed down cell death
440 induction (Figure 6C). For F187, the F187T mutant exhibited weaker cell death, whilst
441 F187W was not significantly different from wild-type, indicating an aromatic residue is
442 important at this site. The cell death caused by the W160H mutant was also weaker
443 than the wild-type. Together, these results demonstrate that changes in NADase
444 activity altered the function of HopAM1 *in planta*.
445
446 **Discussion**
447
448 Recent research has brought the role of $NAD^+$-derived small molecules in host-
449 pathogen interactions into focus. It has become clear that the NADase activity
450 possessed by plant TIR proteins is essential for immune signaling (Bayless and
451 Nishimura, 2020). However, how pathogens may manipulate this key component of
452 immune system for the benefit of disease development is largely unknown. Harnessing
453 the pangenomic diversity and wealth of genetic resources of the model bacterial
454 pathogen *P. syringae*, we were able to conduct a near saturated search of NADases
455 and identified the NADase effector repertoire in this species complex. Further
456 structural analysis and experimental validation provide novel insight into the functional
457 diversity of NADase enzymes. Thus, this research advances our understanding of
458 $NAD^+$ manipulation as a important virulence strategy.
459
460 For NADase identification, we employed both a HMMER and HHsearch. Combining
461 both methods for domain identification was important because both approaches have
462 their own pros and cons. The HMMER approach searched all 2,867,287 *P. syringae*
463 protein sequences with high sensitivity and allowed specific searching of all alleles
464 within each of the > 35,000 orthogroups for similarity to a curated set of sequences of
465 defined domains. However, this analysis relied on what is already in the pfam-seed
466 alignment and may have missed remote homologues that do not share significant
467 sequence similarity (Pereira and Alva, 2021). For example, the HopAG1 ART domain,
468 OG5256, OG18195, OG4578, and OG18056 were not identified by the HMMER
469 search. The HHsearch approach used HMM-HMM comparisons and added secondary
470 structure information to identify hits in a database. However, this approach relies on

471 extracting hits annotated as the enzymes of interest and thus depended on accurate
472 annotation of database entries. In addition, we only ran the consensus sequence of
473 each orthogroup due to it being computationally intensive, so could miss variation
474 within orthogroups. Our results clearly demonstrate the power of using a combination
475 of methods for domain identification. This pipeline could readily be applied to identify
476 any protein or enzyme families of interest. With the advent of rapid and accurate
477 protein structural prediction, integration of Alphafold2 structural models in functional
478 annotation pipelines such as this one will aid predictions where sequence-based
479 approaches fail to pick up remote similarities in structure alone.
480
481 As a major metabolite and redox carrier, $NAD^+$ regulates various cellular processes.
482 Consistently, we found a large amount of NADases encoded in each *P. syringae*
483 genome, performing both house-keeping and accessory functions. Importantly, some
484 NADases are specifically found in the primary phylogroups that are major plant
485 pathogens, indicating that they may have specific roles in virulence or adaptation
486 towards host environments. Although we focused on identifying T3Es in this study, it
487 would be interesting to determine if any of these non-T3E NADases are *hrp*-regulated
488 and thus may also contribute to pathogenesis. For example, Drabinska et al. (2020)
489 identified multiple NUDIX enzymes in the animal opportunistic pathogen *P. aeruginosa*
490 that are involved in virulence, production of the toxin pyocyanin, and resistance to
491 oxidative stress.
492
493 Overall, *P. syringae* has a diverse set of T3Es with putative NADase activities. On
494 average, primary phylogroup strains possess three NADase T3E genes per genome,
495 with most possessing multiple T3Es with different enzymatic activities. Notably, we
496 found a putative novel ART which may be in an operon with three other known T3Es.
497 Within this operon the known effector HopAG1 also possesses both ART and NUDIX
498 domains. We also identified a novel PDE candidate. It has been noted that host
499 metabolism shifts drastically during PstDC3000 infection of *A. thaliana* (Drenichev et
500 al., 2019; Ward et al., 2010). PstDC3000 possesses effectors with NADase activities,
501 including two copies of the TIR effector HopAM1. These effectors may directly
502 contribute to metabolomic changes seen in these previous studies. Previous studies
503 on effector biology have been focused on protein targets in the host cells. Our results
504 point to manipulation of host metabolites as a major virulence target.

505

506 Of the novel T3Es identified, OG18056 is predicted to have similarity to ADPR
507 cyclases, which represents a novel virulence activity. Only eukaroytic ADPR cyclases
508 such as CD38 have been characterized for their roles in physiology and immunity
509 (Hogan et al., 2019). Previous studies have suggested there is limited sequence and
510 structural similarity between TIRs and ADPR cyclases, however the pocket of
511 OG18056 was able to align to both structures suggesting at least some similarity in
512 the folds that make up the catalytic pocket. It will be interesting to identify the
513 substrates and products of this effector and understand how they are related to the
514 virulence activity *in planta.* This effector is specifically found in pathogens of grass
515 species. The presence of nearby mobile elements indicates this effector is likely within
516 a plasmid/genomic island in these strains. A search of the protein against NCBI using
517 BLASTP showed homologues in *Pectobacteriaceae* including plant-associated strains
518 of *Pectobacterium* and *Brenneria* (Supplemental Table S6), reinforcing the horizontal
519 gene transfer hypothesis.

520

521 It has been shown that TIR domains like ADPR cyclases have multiple activities
522 including hydrolase, cyclase and base-exchange (Angeletti et al., 2022; Hogan et al.,
523 2019). Once $NAD^+$ is cleaved, the ADPR may transiently remain in the catalytic pocket
524 to be further modified for example via cyclisation or converted to other products. The
525 residues on the catalytic surface likely dictate the strength of binding, orientation of
526 ADPR and eventual products produced. Very recent structural analyses have shown
527 that various bacterial TIR proteins cyclise ADPR at differing positions on the ribose
528 sugar (Leavitt et al., 2022; Manik et al., 2022). Further investigation of diverse TIRs
529 across kingdoms may lead to the discovery of additional small molecule variants with
530 distinct roles. To add to this, the animal TIR hSARM1 is known to have a range of
531 activities which are regulated by the metabolic state of the cell (Angeletti et al., 2022).
532 How bacterial and plant TIR enzyme activities are regulated remain to be explored.

533

534 We examined the diversity of *P. syringae* TIRs using AlphaFold2-based structural
535 modeling combined with $NAD^+$ docking. Our analysis identified 27 *P. syringae* TIRs
536 that could be activite NADase enzymes and detected a high degree of diversity at the
537 $NAD^+$-interacting residues, supporting that these enzymes could produce different
538 products involved in anti-viral defence, metabolic pathways and pathogenesis. There

539 are some caveats to this analysis: for example TIR domain proteins often naturally
540 form oligomers (Wan et al., 2019), so our monomeric structural models may be
541 missing information about pockets/active site interactions that appear upon
542 oligomerisation. In addition, purely *in silico* structural analysis may miss biologically
543 relevant conformational changes (Hofer et al., 2016). However, this analysis can allow
544 us to generate testable hypotheses. For example, conducting the docking analysis
545 across diverse structures allowed us to generate a list of potentially important residues
546 for functional analysis. Encouragingly, recent structural analysis of plant and bacterial
547 TIRs (Burdett et al., 2021; Manik et al., 2022) detected similar positions that are
548 involved in binding $NAD^+$ *in vitro*. Furthermore, specific substitutions of these residues
549 led to functional changes in HopAM1, confirming the robustness of our analysis.
550
551 Several interesting observations were made through our HopAM1 mutagenesis
552 analysis: the F187T mutant was slower at inducing cell-death. This is consistent with
553 the recent finding that aromatic amino acids at positions corresponding to F187 in
554 other bacterial TIRs is specifically important for the cyclase activity (Manik et al., 2022).
555 Intriguingly, the mutant HopAM1(F187A) was not found to change cell death induction
556 in yeast (Eastman et al., 2021). Similarly, the F95 mutants (F95H and F95W) and
557 W160H triggered weaker cell death. Perhaps the enzymatic activity was reduced due
558 to the importance of these residues for substrate binding. An alternative hypothesis is
559 that the activity is altered and thus less of the 'cell-death' inducing molecule is
560 produced. Mutations F102K, S185K and A97R completely abolished cell death. We
561 were surprised that these mutations led to such drastic phenotypes as the amino acids
562 were changed to those in the corresponding positions in hSARM1 (for S185 and A97)
563 or hCD38 (for F102), and thereby should not abolish the enzymatic activity. It would
564 be interesting to see if the loss of cell-death observed for these residues is due to a
565 change in activity, such as the specific products produced. In summary, our results
566 support the idea that different TIR/ADPR cyclase active sites vary and subtle
567 differences in the amino acids across the sites modulate the enzymatic reaction and
568 the phenotypic consequences.
569
570 A key question is why would bacterial pathogens produce TIR effectors that may
571 trigger cell death? HopAM1 is known to trigger plant cell death in an EDS1-
572 independent manner (Choi et al., 2017), thus differing from most plant immune

573 receptor TNLs, which signal through EDS1 (Lapin et al., 2020). Phylogenomic analysis
574 has revealed some plant TIR proteins are also EDS1-independent (Johanndrees et
575 al., 2021). It is intriguing to speculate that variation in key active site residues result in
576 the differences in products of these TIR proteins, leading to distinct phenotypes. How
577 these effector produced molecules trigger cell death whilst promoting virulence and if
578 they can disrupt plant TIR signalling pathways through molecular mimicry are
579 important future questions. Our research paved the way of conducting such
580 investigation in the future.
581
582 **Methods**
583
584 **Bacterial strains and plant material**
585 Strains and plasmids used in this study are listed in Supplemental Table S7.
586 *Pseudomonas* strains used in this study include *P. syringae* pv. tomato strain DC3000
587 (PstDC3000), the T3S mutant Δ*hrcC* (Yuan and He, 1996), and the effector-less
588 mutant D36E (Wei et al., 2015). *P. coronafaciens* NCPPB 2397 (equivalent to ICMP
589 4457, genome assembly GCA_001400695) was used to clone the novel T3E
590 OG18056. Antibiotics were used at the following concentrations kanamycin: 50 µg/mL,
591 rifampicin: 50 µg/mL, carbenicillin: 100 µg/mL, gentamycin 50 µg/mL. These strains
592 were used to inoculate *Nicotiana benthamiana* and *Arabidopsis thaliana* ecotype col-
593 0 to examine cell death-triggering activities of HopAM1 and its mutants. *Agrobacterium*
594 *tumerfaciens* strain GV3101 was used for *Agrobacterium*-mediated transient
595 expression in *N. benthamiana*.
596
597 *N. benthamiana* plants were grown in a controlled growth room with 16:8 light:dark
598 conditions at 22 °C, 80% humidity. *A. thaliana* plants were grown in a growth chamber
599 with 10:14 light:dark conditions at 20 °C, 80% humidity. Five week old *N. benthamiana*
600 and four week old *A. thaliana* were used for agro-infiltration and *P. syringae*
601 inoculations.
602
603 **Plasmid construction**
604 Golden gate cloning (Engler et al., 2008) was used to generate constructs for transient
605 expression of effectors in plants. Level 0 parts included: 35S long promoter, CDSNS

606 (no stop) acceptor, 3xFLAG C-terminal tag, 35S terminator. The CDS were ordered
607 from Twist Bioscience and PCR amplified using Phusion HR polymerase
608 (ThermoFisher) to add golden gate compatible overhangs. Primers used in this study
609 are presented in Supplemental Table S8. CDS were inserted into the level 0 CDSNS
610 acceptor using one-pot digestion-ligation reaction with the restriction enzyme BpiI-HF
611 (New England Biolabs). Level 0 fragments were then assembled into the *in planta*
612 expression vector pICH47732.
613
614 Effector genes were also cloned into pUCP20TK for expression in *P. syringae*. For
615 *OG18056*, the genomic DNA containing CDS and its native promoter (250 bp
616 upstream of the start codon) was amplified from *P. coronafaciens* NCPPB 2397 with
617 the addition of a C-terminal HA tag in the reverse primer. For *hopAM1*, the wild-type
618 allele (encoded by PstDC3000) and nine mutants were synthesized with C-terminal
619 HA tags (Twist Bioscience) and PCR amplified to add overhangs for infusion cloning
620 (Takara). The *hopAM1* promoter sequence (207 bp upstream of the start codon) was
621 PCR amplified from PstDC3000 gDNA. Infusion cloning was used to insert promoter
622 and CDS fragments in reverse orientation to the *lacZ* promoter in the pUCP20TK
623 vector after linearisation of the vector with BamH1 and EcoR1 (New England Biolabs).
624 For generation of the E305A mutant of OG18056, a site-directed mutagenesis
625 approach using infusion was performed, splitting the gene and promoter fragment into
626 two PCR products for cloning with the mutation introduced in primers R1 and F2. All
627 constructs were confirmed by sanger sequencing. The recombinant plasmids were
628 electroporated into *P. syringae* as described in Choi et al. (2006) apart from recovery
629 growth was for 2 hours at 28 °C, 220 rpm.
630
631 **Agro-infiltration in *N. benthamiana***
632 *A. tumefaciens* GV3101 with various constructs was streaked from glycerol stocks
633 onto LBA plates containing appropriate antibiotics. Two-day old bacterial lawns were
634 resuspended in sterile distilled water and washed twice by spinning at 3000 rpm for
635 10 minutes. The cells were resuspended in $MgCl_2$-2-(N-morpholino)ethanesulfonic
636 acid (MES) buffer (10 mM $MgCl_2$, 10 mM MES, pH 5.6) to a final concentration of
637 $OD_{600}$=1.0 before adding acetosyringone to a final concentration of 150 μM. Bacteria
638 were incubated at room temperature (22 °C) for 3 hours before combining in a 1:1 ratio

639 with the strain carrying the viral RNA silencing suppressor P19, meaning the final
640 $OD_{600}$ of each *Agrobacterium* strain was 0.5. After *Agro*-infiltration, plants were
641 monitored for cell death symptoms for 3-5 days. Images were taken under natural and
642 UV light. Protein expression was confirmed by immunoblotting using total proteins
643 extracted from 1 cm leaf discs at 2 days post inoculation. Leaf discs were immediately
644 frozen in liquid nitrogen and stored at -80 °C. To extract proteins, 100 µL of protein
645 extraction buffer (50 mM Tris-HCl (pH 7.5), 150 mM NaCl, 1 mM EDTA, 0.1% Triton
646 X-100) was added and the discs were ground with a micropestle whilst on ice. Crude
647 plant material was removed by centrifugation at 11,000 x g for 15 minutes and 60 µL
648 of the supernatant was combined with 30 µL 3X Laemmli buffer (Laemmli, 1970) with
649 1x cOmplete EDTA-free protease inhibitor cocktail (ThermoFisher) and boiled at 95°C
650 for 5 minutes. Immunoblotting was performed as described previously (Zhou et al.,
651 2009). An anti-FLAG antibody conjugated to horseradish peroxidase (Sigma) was
652 used at 1:2000.
653
654 **Effector expression and secretion analysis**
655 To confirm that novel effector protein OG18056 was induced in Hrp-inducing minimal
656 medium and secreted in a T3S-dependent manner, PstDC3000 and the Δ*hrcC* mutant
657 carrying pUCP20TK::OG18056-HA were used for protein extraction. A protocol based
658 on (Vinatzer et al., 2005) was utilised to extract secreted proteins from supernatents.
659 The protocol was modified to extract from 8 mL of bacterial supernatant (rather than 2
660 mL). Immunoblotting was performed as in Zhou et al. (2009) using anti-HA from rat
661 (Roche) at 1:1000, followed by a secondary anti-rat antibody conjugated to
662 horseradish peroxidase (sc-2750, Santa Cruz) at 1:2000. The same protocol without
663 supernatant extractions was used to confirm the expression of OG18056 and HopAM1
664 in PstDC3000 D36E used in bacterial infection assays.
665
666 ***In planta Pseudomonas* assays**
667 PstDC3000 D36E carrying specific effector alleles or the pUCP20TK empty vector
668 were grown from glycerol stock for 2 days on agar plates at 28 °C, and the lawn was
669 resuspended in 10 mM $MgCl_2$ to the required optical density for inoculation. Cell
670 suspensions were syringe-infiltrated into *N. benthamiana* leaves at a concentration of
671 $OD_{600}$ 0.4 (~2 x $10^8$ cfu/mL). A lower concentration at 5 x $10^6$ cfu/mL was used to

672 inoculate *A. thaliana*. Symptom development was recorded over several days and
673 pictures taken 3 days post inoculation. For bacterial population assays, inoculum was
674 prepared at 5 x $10^5$ cfu/mL for *A. thaliana*. Bacteria were enumerated after 0 and 3
675 days by plating a dilution series on Kings B agar supplemented with rifampicin and
676 kanamycin.
677
678 **Genome retrieval and annotation**
679 2,437 *P. syringae* (taxid136849) genomes were download from NCBI on November
680 18th, 2020. Genomes were grouped into 806 clusters showing ≥ 99.95% ANI using
681 FastANI v1.32 (Jain et al., 2018). One genome per cluster was chosen based on the
682 assembly with the lowest number of contigs. Genomes were filtered using an approach
683 similar to Levy et al. (2018), removing those with ≥ 1000 contigs and an N50 value
684 lower than 40,000 bp computed with Quast (Gurevich et al., 2013). Finally, CheckM
685 (Parks et al., 2015) was used to select genomes with ≥ 95% complete and < 5%
686 contamination, leaving 531 genomes. Using a cut-off of ≥ 80% ANI, all but two
687 genomes are clustered into a single group. These two genomes (GCA_ 900582625
688 and GCA_900573885) were kept as out-groups.

689 Genome annotation was performed using PROKKA (Seemann, 2014) and Orthofinder
690 (Emms and Kelly, 2019) was used to define orthogroups. To generate a core genome
691 phylogeny, 409 single copy orthogroups present in all genomes were aligned using
692 ClustalW (Thompson et al., 1994) with ends trimmed by Gblocks (Castresana, 2000).
693 Sequences were then concatenated into a 68,325 bp alignment, converted to the
694 phylip format and input into IQ-TREE2 (Minh et al., 2020) with parameters JTT+I+G
695 and 1000 bootstraps.

696 **Identification of Type III secretion system (T3S) and known Type III effectors**
697 **(T3Es)**
698 To identify genomes containing a canonical *hrp* T3S, a BLAST-based approach was
699 taken similar to that described in Dillon et al. (2019). T3S proteins from PstDC3000,
700 *P. syringae* pv. *syringae* B728A, and *P. viridiflava* LP23.1a (Supplemental Table S9
701 lists accession IDs) were used in a tBLASTn to query each genome. A genome was
702 determined to putatively encode a *hrp* T3S if it had a hit to every query with > 30%
703 length and > 30% identity for at least one of the three T3S inputs. A similar approach

704 was taken to determine which orthogroups corresponded to known T3E families in *P.*
705 *syringae*. A set of T3E protein sequences from pseudomonas-syringae.org was used
706 as input to query all orthogroups with BLASTp. Orthogroups containing proteins with
707 hit identities of 100% and E-value < $1x10^{-10}$ were determined to be those
708 corresponding to known T3Es.
709
710 **NADase T3E prediction**
711 The procedure employed to identify nucleosidase candidates in *P. syringae* is
712 presented in Figure 2A. HMMER (http://hmmer.org/) was used to search for proteins
713 carrying domains that are associated with different NADases. Pfam seed alignments
714 for enzyme families (listed in Supplemental Table S1) were obtained from Pfam
715 (http://pfam.xfam.org/) (downloaded on December 1st, 2020). The script hmmbuild was
716 used to create a HMM profile for each seed alignment. The command hmmsearch was
717 then used to screen all *P. syringae* proteins. HMMER results were filtered based on a
718 tolerant bit-score of ≥ 15 (Kloosterman et al., 2020) and grouped by orthogroup.
719 Orthogroups with positive hits were further filtered to remove those in which less than
720 5% of the orthogroup members were a hit as these rare hits may not represent the
721 orthogroup function.
722
723 The program HHsearch (Soding et al., 2005) was also used for each orthogroup to
724 predict similarity to proteins in the PDB database (downloaded on October 28th, 2021).
725 First, a multi-sequence alignment (MSA) was generated using ClustalW and a
726 consensus sequence for each orthogroup was generated using hhcon. Next, the
727 secondary structure of the consensus protein sequence was predicted by PSIPRED
728 and added to the alignment (Jones, 1999) before running HHsearch. Bash scripting
729 was used to extract candidates with hits towards NADase enzymes in the database
730 using a cutoff of ≥ 80% probability score. Two additional hits per protein with non-
731 overlapping regions were also identified, allowing proteins with multiple NADase
732 domains to be identified.
733
734 Candidate orthogroups predicted with HMMER or HHsearch were next screened with
735 EffectiveT3 (Eichinger et al., 2016) to determine if any could be T3Es. Orthogroups
736 containing hits with a score ≥ 0.9 were further analyzed for putative *hrp* box sequences

737 in their promoter region (within 1000 bp upstream of the protein-coding sequence)
738 using the program FIMO (Grant et al., 2011). The background model was created
739 using all promoters of all orthogroups and the *hrp* box sequence GGAACC(15-
740 17N)CCACNNA was used as the input. The program was run three times to account
741 for different size spacers.
742
743 Candidate T3Es were manually filtered based on the percentage of sequences within
744 the orthogroup predicted to be an effector (≥ 50%) and the percentage of these
745 sequences that contained a possible *hrp*-box promoter (≥ 25%). Orthogroups that
746 were only present in genomes without a predicted *hrp* T3S were removed. Candidates
747 T3Es were then manually examined to determine if they had characteristic N-terminal
748 characteristics associated with *P. syringae* T3Es (Guttman et al., 2002; Petnicki-
749 Ocwieja et al., 2002). The consensus sequence of each orthogroup was examined for:
750 1) a high percentage of serines in the first 50 amino acids; 2) an aliphatic amino acid
751 in positions 3 or 4; and 3) a lack of negatively charged residues within the first 12
752 positions. The genomic locations of each T3E candidate gene were also manually
753 examined using Geneious Prime 2022.0.1 to examine gene neighbourhoods
754 (https://www.geneious.com).
755
756 **Protein structure prediction and alignment**
757 Structural prediction was conducted using ColabFold AlphaFold2 batch with MMseqs2
758 (Mirdita et al., 2022). The pipeline developed to identify the catalytic pocket of each
759 TIR protein and predict residues involved in $NAD^+$ binding is illustrated in Figure 5A.
760 For structural alignments, PDB files were aligned using fr-tm-align (Pandit and
761 Skolnick, 2008). Aligned residues, root-mean-square deviation (RMSD) scores, and
762 alignment lengths were extracted using bash scripting. To build a dendrogram based
763 on structural similarity, RMSD values from pairwise alignments were extracted and
764 standardised by dividing with alignment length. These values were then converted to
765 a distance matrix using R software. This distance matrix was used as the input to the
766 program fitch within phylip (v3.69) (Felsenstein, 2009). The order of species was
767 randomised in 100 independent runs.
768

769 Alignments were also conducted between each full-length *P. syringae* TIR protein and
770 the known NADase domain of the human TIR protein hSARM1 (structure 6O0R).
771 Residues in the 561-700 aa fragment of hSARM1 were extracted with PyMOL to
772 create a PDB file of just the TIR domain to be used in the alignments. To obtain the
773 corresponding positions in CD38, alignments were also performed with structures
774 6VUA and 1R12.
775
776 **Molecular docking of $NAD^+$**
777 Autodock Vina v1.2.3 (Eberhardt et al., 2021) was used for molecular docking. P2Rank
778 (Krivak and Hoksza, 2018) was first used to predict catalytic pocket sites. Output files
779 were processed with python to extract the pocket containing the catalytic residues that
780 aligned with hSARM1-TIR. Pocket coordinates were added to the Vina config file for
781 the docking run. The $NAD^+$ ligand was downloaded in 3D format from
782 https://zinc20.docking.org (Irwin et al., 2020) and converted to PDBQT format using
783 the Autodock Vina prepare_ligand script. The Radius of Gyration was calculated and
784 multiplied by 2.9 using python to generate the appropriate sized grid for ligand binding
785 (Feinstein and Brylinski, 2015). Autodock Vina was then ran with exhaustiveness of
786 32 to produce eight possible models.
787
788 For each docked model, the protein and docked ligand PDBQT files were converted
789 back to PDB using open babel (O'Boyle et al., 2011) and concatenated to generate a
790 single file. This was then input into plip (v2.2.2) (Salentin et al., 2015) with default
791 parameters to predict bonds between $NAD^+$ and the protein. The plip output files of all
792 eight possible docked conformations were then combined to obtain all possible protein
793 residues that may bind to $NAD^+$ regardless of its orientation within the active site.
794
795 **Figure creation**
796 PyMOL (https://pymol.org/2/) was used for visualisation of protein structures. The Pro-
797 origami online server was used for protein topology diagrams (Stivala et al., 2011).
798 WebLogo (http://weblogo.threeplusone.com/) was used to generate a sequence logo
799 of residues at particular positions in *P. syringae* TIR/ADPR cyclase proteins. Biorender
800 (BioRender.com) was used to create diagrams. All other figures were created using R
801 software (R.Core.Team, 2020). Specifically, the packages ape (Paradis and Schliep,

2019), phangorn (Schliep, 2011), ggplot2 (Wickham, 2016), ggtree (Guangchuang, 2020) and reshape (Wickham, 2007).

**Statistical analysis**

Analysis of variance (ANOVA) was used to statistically compare cell death symptoms over time after *Agro*-infiltration as well as population counts of *P. syringae* from *Arabidopsis*. Tukey-HSD significance groups were extracted using R packages emmeans (Lenth, 2022) and the cld function within agricolae (de Mendiburu and Yaseen, 2020) .

**Acknowledgments:** We thank Dr. Alan Collmer for providing the *P. syringae* D36E mutant and Ma lab members for discussions and technical support. We thank Dan MacLean and George Deeks for bioinformatic analysis support. **Funding:** W.M. is supported by Gatsby Charitable Foundation and UKRI BBSRC Grant BBS/E/J/000PR9797. **Author Contributions:** W.M. and M.T.H. conceived the project. M.T.H. did the experiments and analyzed the data. W.M. and M.T.H. wrote the manuscript. **Competing Interests:** The authors declare no competing interests.

**Data and material availability:** All code are available at https://github.com/michhulin/Pseudomonas. Materials are available from W.M. upon request under a materials transfer agreement with the Sainsbury Laboratory.

837
838
839
840
841
842
843 **Table 1. Characteristics of enzymes that can cleave $NAD^+$ including defining folds,**
844 **catalytic residues, known substrates and products.**

| Group | Folds | Catalytic residues | Bond | Known role(s) | Activity | Substrates | Products | References |
|---|---|---|---|---|---|---|---|---|
| NUDIX | Nudix fold, beta-grasp domain, loop-helix-loop | RExxEE | Pyrophosphate/ phoshodiester | Hydrolase, removal of post-translational modifications | Hydrolysis | Pyro-phosphate bonds e.g. NADH | Various e.g. NMN, AMP | Srouji et al., (2017) |
| PDE | Phospho-esterase fold | H-H | Phosphodiester | Hydrolase | Hydrolysis | Various. cNMPs e.g. cAMP, DNA, RNA | various e.g. AMP | Turko et al. (1998), Akturk et al., (2018) |
| ART | ADP-ribosylating toxin turn-turn (ARTT) loop, phosphate-nicotinamide (PN) loop | ExE | N-glycosidic bond | Post-translation modification, DNA/RNA modification, NAD+ glycohydrolase | Hydrolysis, ribosyltransferase | NAD+ | ADPR, NAM | Menetrey et al. (2008), Aravind et al. (2015) |
| SIR | Rossmann-fold domain | N, H | N-glycosidic bond | Post-translation modification | Hydrolysis, deacetylase, ribosyltransferase | NAD+ | o-acetyl-ADPR, NAM | Sanders et al., (2010), Yuan and Marmorstein (2012) |
| TIR | Central parallel beta-sheet (βA-E) surrounded by alpha helices (αA–E) | E | N-glycosidic bond | Hydrolase | Hydrolysis, cyclase, base-exchange | NAD, NADP, NADH | ADPR, cADPR, v-cADPR, NAM, ADPRP, cADPRP, NAAD, NAADP, pRib-ADP, pRib-AMP, gcADPR, ADPR-ATP, diADPR | Ve et al. (2015),Essuman et al., (2017), Essuman et al., (2018), Angeletti et al., (2022), Huang et al. (2022), Leavitt et al. (2022), Jia et al. (2022) |
| ADPR cyclase | Central cleft between N and C-terminal domains forms active site | E | N-glycosidic bond | Hydrolase | Hydrolysis, cyclase, base-exchange | NAD, NADP, NADH, ADPR, Adenine | ADPR, cADPR, v-cADPR, NAADP, NAM, AP2A isomers, diADPR | Aarhus et al. (1995), Basile et al. (2005), Graeff et al., (2009), Grahnert et al. (2011) |
| NH | Central parallel beta-sheet surrounded by alpha helices | D-D | N-glycosidic bond | Hydrolase | Hydrolysis | Nucleosides, e.g. iP-riboside 5′-monophosphate | iP, PR | Garau et al. (2010), Li et al. (2013), Hann et al., (2014), Drenichev et al., (2018) |

845
846
847

848 **Table 2. Numbers of putative NADase enzymes predicted by HHsearch and HMMER in**
849 **the *P. syringae* pangenome.**

| | HHsearch | HHsearch unique | HMM | HMM unique | Shared | Complete | Core | Accessory |
|---|---|---|---|---|---|---|---|---|
| TIR/ ADPR cyclase | 66 | 34 | 34 | 2 | 32 | 68 | 5 | 63 |
| NUDIX/ Pyrophosphatase | 109 | 81 | 30 | 2 | 28 | 111 | 38 | 73 |
| ART | 140 | 112 | 34 | 6 | 28 | 146 | 28 | 118 |
| PDE | 226 | 186 | 40 | 0 | 40 | 226 | 53 | 173 |
| NH | 8 | 3 | 5 | 0 | 5 | 8 | 2 | 6 |
| SIR | 15 | 12 | 3 | 0 | 3 | 15 | 2 | 13 |
| Total | 564 | 428 | 146 | 10 | 136 | 574 | 128 | 446 |

850

851

852 **Table 3. Predicted number of T3Es for each enzyme family in the *P. syringae***
853 **pangenome.**

| Group | Total | EffectiveT3[a] | High frequency effectors[b] | T3SS+[c] and *hrp* promoter[d] | Manual filtering[e] |
|---|---|---|---|---|---|
| TIR/ADPR cyclase | 68 | 36 | 14 | 7 | 3 |
| NUDIX/ Pyrophosphatase | 111 | 50 | 13 | 8 | 1 |
| ART | 146 | 74 | 26 | 14 | 7 |
| PDE | 226 | 114 | 43 | 20 | 1 |
| NH | 8 | 5 | 2 | 1 | 1 |
| SIR | 15 | 6 | 2 | 1 | 0 |
| Total | 574 | 285 | 100 | 51 | 13 |

854
855 a; Candidates with members scoring over 0.90 with EffectiveT3
856 b; Candidates where ≥ 50% of the orthogroup sequences were annotated as an effector
857 c; Candidates with effectors present in at least 1 genome with a canonical T3SS predicted
858 d; Candidates with ≥ 25% of the sequences possessed a proceeding *hrp*-box promoter
859 within 1000 bp (purposely set low in the case of possible operons)
860 e; Remaining candidates were manually checked, those within operons of non-effector
861 genes, or with a *hrp*-box promoter within other CDS or > 400bp away from the start codon
862 were removed
863
864

865 **Table 4. Known NADase T3Es and predicted candidates in *P. syringae.***

| Group | Ortho-group | No. genes | No. effectors | % Effectors | No. *hrp* promoter | % *hrp* promoter | No. genomes | No. T3SS+ genomes | % T3SS+ genomes | Notes | Secretion signal score (out of 3) |
|---|---|---|---|---|---|---|---|---|---|---|---|
| **ART** | OG4303 | 339 | 332 | 98 | 299 | 90 | 188 | 187 | 99 | HopF/BB | 2 |
| **ART** | OG5256 | 144 | 130 | 90 | 38 | 29 | 37 | 35 | 95 | **Novel** | **3** |
| **ART** | OG5397 | 133 | 91 | 68 | 54 | 59 | 46 | 46 | 100 | HopO1 | 3 |
| **ART** | OG5686 | 112 | 103 | 92 | 91 | 88 | 87 | 87 | 100 | AvrRpm | 3 |
| **ART** | OG6340 | 69 | 54 | 78 | 53 | 98 | 53 | 53 | 100 | HopS | 3 |
| **ART** | OG9885 | 14 | 14 | 100 | 10 | 71 | 10 | 10 | 100 | HopU1 | 3 |
| **ART** | OG18195 | 3 | 3 | 100 | 3 | 100 | 3 | 3 | 100 | **Novel** | **3** |
| **ART**[a] | OG4463 | 297 | 223 | 75 | 213 | 96 | 213 | 213 | 100 | HopAG1 | 3 |
| **NH** | OG4871 | 195 | 124 | 64 | 121 | 98 | 118 | 117 | 99 | HopQ1 | 2 |
| **NUDIX** | OG4463 | 297 | 223 | 75 | 213 | 96 | 213 | 213 | 100 | HopAG1 | 3 |
| **PDE** | OG4578 | 258 | 214 | 83 | 102 | 48 | 101 | 100 | 99 | **Novel** | **2** |
| **TIR** | OG6638 | 55 | 49 | 89 | 45 | 92 | 38 | 37 | 97 | HopAM1 | 3 |
| **TIR** | OG8567 | 23 | 21 | 91 | 15 | 71 | 14 | 14 | 100 | **Novel** | **2** |
| **TIR** | OG18056 | 3 | 3 | 100 | 3 | 100 | 3 | 3 | 100 | **Novel** | **3** |

866
867 No. genes: number of genes in orthogroup.
868 No. effectors: number of genes within orthogroup that were predicted to encode an effector.
869 % effectors: % orthogroup that may code effector.
870 No. *hrp* promoter: Number of predicted effector genes per orthogroup that had a predicted *hrp* box
871 % *hrp* promoter: % effector genes in orthogroup that had *hrp* promoter.
872 No. T3S+ genomes: Number of genomes encoding the genes in each orthogroup predicted as
873 effectors with a *hrp* box which have the genes required for T3S machinery.
874 % genomes with T3S+: % of effector genes with a *hrp* box per orthogroup that were in T3S+
875 genomes.
876 Secretion signal score: A score from 0-3 based on three previously defined criteria of T3E secretion
877 signals:1) a high % serines; 2) a lack of negative amino acids in the first 12 residues; 3) an aliphatic
878 amino acid at position 3 or 4.
879 [a]Although the main hit of OG0004463 (HopAG1) was a NUDIX domain, a further domain with
880 homology to ART was predicted at a different region of the protein.
881
882

883 **Table 5. Information on the nine putative interacting sites across the catalytic sites of**
884 **TIR/ADPR cyclases with rationale behind mutational strategy.**

| No. *P.s* TIRs interacting | HopAM1 (C?) | SARM1 (Ac) | OG 18056 (?) | hCD38 (Ac) | aCD38 (aC) | Mutants | Outcome | Reasoning | Notes |
|---|---|---|---|---|---|---|---|---|---|
| **17** | F95* | Y568 | W149 | W125 | W77 | H, W | Slower cell death | Change to similar residue to modify activity | Ramakrishnan et al., (2010) changed corresponding residue in SpARC4 cyclase (CD38 homologue) from Y to either W or H and reduced cyclase activity |
| **15** | A97 | R570 | G151 | R127 | G79 | R | No cell death | Change to SARM1/CD38 residue to alter activity | Liu et al., (2009) showed this residue R127 is involved in CD38 binding NAD+ |
| **12** | F102 | S574 | M164 | K129 | Y81 | K | No cell death | Changed to K based on CD38 lack of cyclase and aCD38 having similar hydrophobic residue | Tohgo et al., (1997) reported K129 in CD38 important for cADPR hydrolysis rather than hydrolysis of NAD+. K129 may also be target of ADP-ribosylation to modify the active site Jiang et al. (2013) |
| **11** | W160 | F603 | W263 | W189 | W140 | H | Slower cell death | Change to non-hydrophobic related amino acid to alter binding | W at this position in CD38 is generally important for binding NAD+ (Liu et al. (2009),Wolters et al. (2019) |
| **15** | S185 | K628 | N291 | N217 | R170 | K | No cell death | Change to SARM1 residue K to see if alters activity | Summers et al. (2016) showed K628 in SARM1 is important for activity. |
| **15** | F187* | W638 | T300 | T221 | F174 | T, W | Slower cell death in T mutant | Change to similar residues as in CD38 papers | Graeff et al., (2009) found mutation from F to T reduced cyclase activity of the cyclase aCD38 without drastically changing hydrolase |
| **14** | E191 | E642 | E305 | E226 | E179 | A | None | Act as a control to show mutation expected | Identified catalytic site of TIRs (Essuman et al. (2017); Horsefield et al. (2019; Eastman et al. (2021) |

885
886 A: produces ADPR, C: produces cyclic-ADPR. Lower case is where the activity of lower than the other
887 activity (in uppercase). ? means products are unknown. * For two well studied residues in CD38 these
888 residues in HopAM1 were changed to two different amino acids based on previous work of specifically
889 altering activity.
890

891 **Figure legends**

892

893 **Figure 1. Enzyme families that may hydrolyse $NAD^+$.**

894 The NUDIX (nucleoside diphosphate linked to a variable moiety X) enzymes and
895 phosphodiesterases (PDEs) cleave the pyrophosphate bond. ADP-ribosyltransferases
896 (ART), nucleoside hydrolases (NH), ADPR cyclases, and sirtuins cleave the N-
897 glycosidic bond.

898

899 **Figure 2. Identification of NADases encoded in the *P. syringae* species**
900 **complex.**

901 A) Two approaches based on HMMER and HHsearch respectively were used to
902 predict all seven NAD hydrolyzing enzyme families from the pangenome of *P.*
903 *syringae*.

904 B) NADase genes predicted across the *P. syringae* species complex are mapped onto
905 the maximum-likelihood core genome phylogeny. Numbers of predicted genes from
906 each enzyme family is presented by heatmaps. The phylogeny was generated
907 based on 409 concatenated single copy core genes. The scale shows amino acid
908 substitutions per site. Strains in the primary phylogroups are coloured in red. Due
909 to similarity in enzymatic activity, NUDIX and pyrophosphatase were grouped
910 together, as well as TIR and ADPR cyclase.

911 C) Venn diagrams to show the number of primary phylogroup specific NADase
912 encoding orthogroups (left), orthogroups shared between primary and secondary
913 phylogroups (middle), and orthogroups specific to secondary phylogroups (right).

914

915 **Figure 3. Predicted NADases as type III effectors in *P. syringae*.**

916 A) NADase T3Es predicted across the *P. syringae* species complex are mapped onto
917 the maximum-likelihood core genome phylogeny. Strains in the primary
918 phylogroups are coloured in red. The presence of a canonical *hrp* T3SS is
919 presented as Ring 1 (in green) and the number of known T3E genes encoded in
920 each strain is presented in Ring 2 as a heatmap coloured in a scale of white to blue.
921 Ring 3-7 each represents one of the five NADase enzyme families. Known T3Es
922 with putative ART domains are in order: HopF/BB, HopO1, AvrRpm, HopS, HopU1,
923 HopAG1. Presence of each orthogroup is coloured as in the scale, with grey
924 squares indicating the orthogroup is present but with no *hrp* box in the promoter.

925 B) Mean number of NADase T3Es per phylogroup. The primary phylogroups are
926 labelled with roman numerals, whilst secondary phylogroups correspond to their
927 species number predicted by Average Nucleotide Identity in Supplemental Figure
928 S1. A collapsed version of the core genome phylogeny, with the primary phylogroup
929 clade in red is included for reference.
930
931 **Figure 4. OG18056 is a novel T3E with similarity to ADPR cyclases.**
932 A) Alignment of a structural model of OG18056 predicted by AlphaFold2 (in cyan) with
933 human CD38 (6VUA, in grey) and the TIR domain of human SARM1 (6O0R, 561-
934 700 aa, in light brown). Root-Mean-Square Deviation (RMSD) values and TM-
935 scores are presented using OG18056 as the reference. For visualisation purposes,
936 sequences outside the alignment region were removed and those that did not align
937 within the region are more transparent. The predicted catalytic Glu residues are
938 aligned in three structures and highlighted with a box.
939 B) Immunoblot showing the induction and secretion of OG18056 by *P. syringae*.
940 OG18056-HA was expressed in PstDC3000 or the T3S mutant Δ*hrcC* under its
941 native promoter. The bacteria were cultured in the rich medium Kings B (KB) or a
942 Hrp-inducing minimal medium (HM). Proteins were extracted from cell pellet (cp) or
943 supernatant (sn) and the protein levels of OG18056 were determined by western
944 blotting using an anti-HA antibody. Ponceau S (PS) staining was used as the
945 loading control.
946 C) OG18056 enhanced the virulence of the effectorless mutant PstDC3000 D36E on
947 *Arabidopsis thaliana*. Upper: disease symptom development by D36E carrying the
948 empty vector, OG18056 or OG18056(E305A). Numbers show the number of leaves
949 with symptoms recorded over three independent experiments. Leaves were
950 inoculated with 5 x $10^6$ CFU/ml inoculum and imaged 3 days later. Lower:
951 population count of the D36E transformants in *A. thaliana*. Boxplots show the day
952 0 and day 3 populations in Log CFU/$cm^2$. Individual data points with different colors
953 represent results from three separate experiments. Tukey-HSD significance groups
954 extracted from ANOVA are presented.
955 D) OG18056 and its mutant were expressed under its native promoter in PstDC3000
956 D36E. Immunoblot showing OG18056 and OG18056(E305A) expression when
957 bacteria were grown in Hrp-inducing minimal medium.

958 **Figure 5. Structural analysis revealed diversity in the active site of *P. syringae***
959 **TIR proteins.**
960 A) A bioinformatic pipeline used to generate 3D structure models of candidate
961 NADases and predict $NAD^+$-binding sites and residues.
962 B) A dendrogram based on structural similarity of 42 TIR proteins and the one ADPR
963 cyclase homologue (OG18056) predicted from *P. syringae* pangenome. The
964 dendrogram was built by the phylip program fitch using a distance matrix based on
965 RMSD values from pairwise structural alignments. The RMSD values were
966 normalized by alignment length. The three predicted TIR/ADPR cyclase T3Es are
967 highlighted in red. Mapped onto the dendrogram is information regarding the
968 structural alignment for each protein with hSARM1-TIR. The RMSD with hSARM1
969 is shown with a blue heatmap. A black box indicates that the protein had a
970 glutamate aligning to the catalytic residue E642 in hSARM1-TIR. The $NAD^+$ binding
971 affinity of each protein is also presented.
972 C) Structually equivalent amino acids that aligned to hSARM1-TIR for each *P. syringae*
973 TIR protein. The residues are ordered based on hSARM1-TIR positions and colour-
974 coded by biochemical features. Nine positions that were frequently predicted to bind
975 $NAD^+$ during *in silico* docking are highlighted (also see D), whilst other positions are
976 greyed out. The catalytic Glu (E642 in hSARM1-TIR) is labelled with a star.
977 D) Nine positions were predicted to bind $NAD^+$ in more than ten *P. syringae* TIR
978 proteins. These include residues corresponding the hSARM1 catalytic residue E642
979 (position 9), the nearby residues 628, 637 and 638 (positions 6-8), as well as
980 residues 568, 570, 574, 594 and 603 (positions 1-5), which are further upstream.
981 E) Sequence logo generated for the nine positions that interacted with $NAD^+$ showing
982 frequency of different amino acids in each position. Amino acids are colour-coded
983 as in (C).
984
985 **Figure 6. Characterization of $NAD^+$-binding residues for cell death inducing**
986 **activity of HopAM1.**
987 A) Predicted structural model of HopAM1 docked with $NAD^+$ with residues subjected
988 to mutational analysis highlighted in green. The electrostatic image of the surface
989 of HopAM1 active site is also presented with regions of positive, neutral and
990 negative charge shown in blue, white and red respectively.

991 B) Cell death induced by HopAM1 and its mutants after transient expression in *N.*
992 *benthamiana* by Agro-infiltration. Representative image of a *N. benthamiana* leaf
993 five days post Agro-infiltration (DPI) is presented. The same leaf imaged under
994 ultraviolet light is included to better visualize the cell death lesions. WT: wild-type;
995 EV: empty vector.
996 C) Quantitative analysis of the cell death phenotype induced by various HopAM1
997 mutants. The appearance of cell death for each mutant was monitored at 3, 4, and
998 5 DPI, and scored as either no cell death (in green), weak cell death (limited, patchy
999 appearance, in light brown) and strong cell death covering the whole inoculation
1000 site (dark brown). Statistical groupings of an ANOVA comparing cell death scores
1001 are shown above the graph. These results are from three independent experiments.
1002

1003 **References**


1004 Aarhus, R., Graeff, R.M., Dickey, D.M., Walseth, T.F., and Lee, H.C. (1995). ADP-ribosyl
1005 cyclase and CD38 catalyze the synthesis of a calcium-mobilizing metabolite from NADP. J
1006 Biol Chem *270*, 30327-30333.
1007 Adlung, N., Prochaska, H., Thieme, S., Banik, A., Bluher, D., John, P., Nagel, O., Schulze, S.,
1008 Gantner, J., Delker, C.*, et al.* (2016). Non-host Resistance Induced by the *Xanthomonas*
1009 Effector XopQ Is Widespread within the Genus *Nicotiana* and Functionally Depends on EDS1.
1010 Front Plant Sci *7*, 1796.
1011 Akturk, A., Wasilko, D.J., Wu, X., Liu, Y., Zhang, Y., Qiu, J., Luo, Z.Q., Reiter, K.H., Brzovic, P.S.,
1012 Klevit, R.E.*, et al.* (2018). Mechanism of phosphoribosyl-ubiquitination mediated by a single
1013 *Legionella* effector. Nature *557*, 729-733.
1014 Angeletti, C., Amici, A., Gilley, J., Loreto, A., Trapanotto, A.G., Antoniou, C., Merlini, E.,
1015 Coleman, M.P., and Orsomando, G. (2022). SARM1 is a multi-functional NAD(P)ase with
1016 prominent base exchange activity, all regulated bymultiple physiologically relevant NAD
1017 metabolites. iScience *25*, 103812.
1018 Aravind, L., Zhang, D., de Souza, R.F., Anand, S., and Iyer, L.M. (2015). The natural history of
1019 ADP-ribosyltransferases and the ADP-ribosylation system. Curr Top Microbiol Immunol *384*,
1020 3-32.
1021 Azevedo, M.F., Faucz, F.R., Bimpaki, E., Horvath, A., Levy, I., de Alexandre, R.B., Ahmad, F.,
1022 Manganiello, V., and Stratakis, C.A. (2014). Clinical and molecular genetics of the
1023 phosphodiesterases (PDEs). Endocr Rev *35*, 195-233.
1024 Basile, G., Taglialatela-Scafati, O., Damonte, G., Armirotti, A., Bruzzone, S., Guida, L., Franco,
1025 L., Usai, C., Fattorusso, E., De Flora, A.*, et al.* (2005). ADP-ribosyl cyclases generate two
1026 unusual adenine homodinucleotides with cytotoxic activity on mammalian cells. Proc Natl
1027 Acad Sci U S A *102*, 14509-14514.
1028 Bayless, A.M., and Nishimura, M.T. (2020). Enzymatic Functions for Toll/Interleukin-1
1029 Receptor Domain Proteins in the Plant Immune System. Front Genet *11*, 539.
1030 Burdett, H., Hu, X., Rank, M.X., Maruta, N., and Kobe, B. (2021). Self-association configures
1031 the NAD+-binding site of plant NLR TIR domains. BioRxiv.

1032 Castresana, J. (2000). Selection of Conserved Blocks from Multiple Alignments for Their Use
1033 in Phylogenetic Analysis. Mol Biol Evol *17*, 540–552.
1034 Choi, K.H., Kumar, A., and Schweizer, H.P. (2006). A 10-min method for preparation of highly
1035 electrocompetent *Pseudomonas aeruginosa* cells: application for DNA fragment transfer
1036 between chromosomes and plasmid transformation. J Microbiol Methods *64*, 391-397.
1037 Choi, S., Jayaraman, J., Segonzac, C., Park, H.J., Park, H., Han, S.W., and Sohn, K.H. (2017).
1038 *Pseudomonas syringae* pv. *actinidiae* Type III Effectors Localized at Multiple Cellular
1039 Compartments Activate or Suppress Innate Immune Responses in *Nicotiana benthamiana*.
1040 Front Plant Sci *8*, 2157.
1041 Corda, D., and Di Girolamo, M. (2003). Functional aspects of protein mono-ADP-ribosylation.
1042 The EMBO Journal *22*, 1953–1958.
1043 Coronas-Serna, J.M., Louche, A., Rodriguez-Escudero, M., Roussin, M., Imbert, P.R.C.,
1044 Rodriguez-Escudero, I., Terradot, L., Molina, M., Gorvel, J.P., Cid, V.J.*, et al.* (2020). The TIR-
1045 domain containing effectors BtpA and BtpB from *Brucella abortus* impact NAD metabolism.
1046 PLoS Pathog *16*, e1007979.
1047 de Mendiburu, F., and Yaseen, M. (2020). agricolae: Statistical Procedures for Agricultural
1048 Research.R package version 1.4.0.
1049 Dillon, M.M., Thakur, S., Almeida, R.N.D., Wang, P.W., Weir, B.S., and Guttman, D.S. (2019).
1050 Recombination of ecologically and evolutionarily significant loci maintains genetic cohesion
1051 in the *Pseudomonas syringae* species complex. Genome Biol *20*, 3.
1052 Dong, S., Yin, W., Kong, G., Yang, X., Qutob, D., Chen, Q., Kale, S.D., Sui, Y., Zhang, Z., Dou,
1053 D.*, et al.* (2011). *Phytophthora sojae* avirulence effector Avr3b is a secreted NADH and ADP-
1054 ribose pyrophosphorylase that modulates plant immunity. PLoS Pathog *7*, e1002353.
1055 Drabinska, J., Ziecina, M., Modzelan, M., Jagura-Burdzy, G., and Kraszewska, E. (2020).
1056 Individual Nudix hydrolases affect diverse features of *Pseudomonas aeruginosa*.
1057 MicrobiologyOpen *9*, e1052.
1058 Drenichev, M.S., Bennett, M., Novikov, R.A., Mansfield, J., Smirnoff, N., Grant, M., and
1059 Mikhailov, S.N. (2019). A role for 3'-O-beta-D-ribofuranosyladenosine in altering plant
1060 immunity. Phytochemistry *157*, 128-134.
1061 Duxbury, Z., Wang, S., MacKenzie, C.I., Tenthorey, J.L., Zhang, X., Huh, S.U., Hu, L., Hill, L.,
1062 Ngou, P.M., Ding, P.*, et al.* (2020). Induced proximity of a TIR signaling domain on a plant-
1063 mammalian NLR chimera activates defense in plants. Proc Natl Acad Sci U S A *117*, 18832-
1064 18839.
1065 Eastman, S., Smith, T., Zaydman, M.A., Kim, P., Martinez, S., Damaraju, N., DiAntonio, A.,
1066 Milbrandt, J., Clemente, T.E., Alfano, J.R.*, et al.* (2022). A phytobacterial TIR domain effector
1067 manipulates NAD(+) to promote virulence. New Phytol *233*, 890-904.
1068 Eberhardt, J., Santos-Martins, D., Tillack, A.F., and Forli, S. (2021). AutoDock Vina 1.2.0: New
1069 Docking Methods, Expanded Force Field, and Python Bindings. J Chem Inf Model *61*, 3891-
1070 3898.
1071 Eichinger, V., Nussbaumer, T., Platzer, A., Jehl, M.A., Arnold, R., and Rattei, T. (2016).
1072 EffectiveDB--updates and novel features for a better annotation of bacterial secreted
1073 proteins and Type III, IV, VI secretion systems. Nucleic Acids Res *44*, D669-674.
1074 Emms, D.M., and Kelly, S. (2019). OrthoFinder: phylogenetic orthology inference for
1075 comparative genomics. Genome Biol *20*, 238.
1076 Engler, C., Kandzia, R., and Marillonnet, S. (2008). A one pot, one step, precision cloning
1077 method with high throughput capability. PLoS One *3*, e3647.

1078 Essuman, K., Summers, D.W., Sasaki, Y., Mao, X., DiAntonio, A., and Milbrandt, J. (2017). The
1079 SARM1 Toll/Interleukin-1 Receptor Domain Possesses Intrinsic NAD(+) Cleavage Activity that
1080 Promotes Pathological Axonal Degeneration. Neuron *93*, 1334-1343 e1335.
1081 Feinstein, W.P., and Brylinski, M. (2015). Calculating an optimal box size for ligand docking
1082 and virtual screening against experimental and predicted binding pockets. J Cheminform *7*,
1083 18.
1084 Felsenstein, J. (2009). PHYLIP (phylogeny inference package) version 3.69. ( Seattle (WA):
1085 Department of Genome Sciences, University of Washington).
1086 Fu, Z.Q., Guo, M., Jeong, B.R., Tian, F., Elthon, T.E., Cerny, R.L., Staiger, D., and Alfano, J.R.
1087 (2007). A type III effector ADP-ribosylates RNA-binding proteins and quells plant immunity.
1088 Nature *447*, 284-288.
1089 Fuchs, E.L., Brutinel, E.D., Klem, E.R., Fehr, A.R., Yahr, T.L., and Wolfgang, M.C. (2010). In
1090 vitro and in vivo characterization of the *Pseudomonas aeruginosa* cyclic AMP (cAMP)
1091 phosphodiesterase CpdA, required for cAMP homeostasis and virulence factor regulation. J
1092 Bacteriol *192*, 2779-2790.
1093 Gallego-Jara, J., Ortega, A., Lozano Terol, G., Sola Martinez, R.A., Canovas Diaz, M., and de
1094 Diego Puente, T. (2021). Bacterial Sirtuins Overview: An Open Niche to Explore. Front
1095 Microbiol *12*, 744416.
1096 Garau, G., Muzzolini, L., Tornaghi, P., and Degano, M. (2010). Active site plasticity revealed
1097 from the structure of the enterobacterial N-ribohydrolase RihA bound to a competitive
1098 inhibitor. BMC Structural Biology *10*.
1099 Gay, N., and Keith, F. (1991). *Drosophila* Toll and IL-1 receptor. Nature *351*, 355-256.
1100 Ghosh, J., and Caparon, M.G. (2006). Specificity of *Streptococcus pyogenes* NAD(+)
1101 glycohydrolase in cytolysin-mediated translocation. Mol Microbiol *62*, 1203-1214.
1102 Gomila, M., Busquets, A., Mulet, M., Garcia-Valdes, E., and Lalucat, J. (2017). Clarification of
1103 Taxonomic Status within the *Pseudomonas syringae* Species Group Based on a
1104 Phylogenomic Analysis. Front Microbiol *8*, 2422.
1105 Graeff, R., Liu, Q., Kriksunov, I.A., Kotaka, M., Oppenheimer, N., Hao, Q., and Lee, H.C.
1106 (2009). Mechanism of cyclizing NAD to cyclic ADP-ribose by ADP-ribosyl cyclase and CD38. J
1107 Biol Chem *284*, 27629-27636.
1108 Grahnert, A., Grahnert, A., Klein, C., Schilling, E., Wehrhahn, J., and Hauschildt, S. (2011).
1109 NAD+: A modulator of immune functions. Innate Immunity *17*, 212-233.
1110 Grant, C.E., Bailey, T.L., and Noble, W.S. (2011). FIMO: scanning for occurrences of a given
1111 motif. Bioinformatics *27*, 1017-1018.
1112 Guangchuang, Y. (2020). Using ggtree to Visualize Data on Tree-Like Structures. Current
1113 Protocols in Bioinformatics *69*, e96.
1114 Gurevich, A., Saveliev, V., Vyahhi, N., and Tesler, G. (2013). QUAST: quality assessment tool
1115 for genome assemblies. Bioinformatics *29*, 1072-1075.
1116 Guttman, D.S., Vinatzer, B.A., Sarkar, S.F., Ranall, M.V., Kettler, G., and Greenberg, J.T.
1117 (2002). A Functional Screen for the Type III (Hrp) Secretome of the Plant Pathogen
1118 *Pseudomonas syringae*. Science *295*, 1722-1725.
1119 Hann, D.R., Dominguez-Ferreras, A., Motyka, V., Dobrev, P.I., Schornack, S., Jehle, A., Felix,
1120 G., Chinchilla, D., Rathjen, J.P., and Boller, T. (2014). The *Pseudomonas* type III effector
1121 HopQ1 activates cytokinin signaling and interferes with plant innate immunity. New Phytol
1122 *201*, 585-598.

1123 Hofer, K., Li, S., Abele, F., Frindert, J., Schlotthauer, J., Grawenhoff, J., Du, J., Patel, D.J., and
1124 Jaschke, A. (2016). Structure and function of the bacterial decapping enzyme NudC. Nat
1125 Chem Biol *12*, 730-734.
1126 Hogan, K.A., Chini, C.C.S., and Chini, E.N. (2019). The Multi-faceted Ecto-enzyme CD38: Roles
1127 in Immunomodulation, Cancer, Aging, and Metabolic Diseases. Front Immunol *10*, 1187.
1128 Horsefield, S., Burdett, H., Zhang, X., Manik, K.M., Shi, Y., Chen, J., Qi, T., Gilley, J., Lai, J.S.,
1129 Rank, M.X.*, et al.* (2020). NAD + cleavage activity by animal and plant TIR domains in cell
1130 death pathways. Science *365*, 793-799.
1131 Huang, S., Jia, A., Song, W., Hessler, G., Meng, Y., Sun, Y., Xu, L., Laessle, H., Jirschitzka, J.,
1132 Ma, S.*, et al.* (2022). Identification and receptor mechanism of TIR-catalyzed small molecules
1133 in plant immunity. BioRxiv.
1134 Irwin, J.J., Tang, K.G., Young, J., Dandarchuluun, C., Wong, B.R., Khurelbaatar, M., Moroz,
1135 Y.S., Mayfield, J., and Sayle, R.A. (2020). ZINC20-A Free Ultralarge-Scale Chemical Database
1136 for Ligand Discovery. J Chem Inf Model *60*, 6065-6073.
1137 Jain, C., Rodriguez-R, L., Phillippy, A.M., Konstantinidis, K.T., and Aluru, S. (2018). High
1138 throughput ANI analysis of 90K prokaryotic genomes reveals clear species boundaries. Nat
1139 Commun *9*, 5114.
1140 Jia, A., Huang, S., Song, W., Wang, J., Meng, Y., Sun, Y., Xu, L., Laessle, H., Jirschitzka, J., Hou,
1141 J.*, et al.* (2022). TIR-catalyzed ADP-ribosylation reactions produce signaling molecules for
1142 plant immunity. BioRxiv.
1143 Jiang, H., Sherwood, R., Zhang, S., Zhu, X., Liu, Q., Graeff, R., Kriksunov, I.A., Lee, H.C., Hao,
1144 Q., and Lin, H. (2013). Identification of ADP-ribosylation sites of CD38 mutants by precursor
1145 ion scanning mass spectrometry. Anal Biochem *433*, 218-226.
1146 Johanndrees, O., Baggs, E.L., Uhlmann, C., Locci, F., Läßle, H.L., Melkonian, K., Käufer, K.,
1147 Dongus, J.A., Nakagami, H., Krasileva, K.V.*, et al.* (2021). Differential EDS1 requirement for
1148 cell death activities of plant TIR-domain proteins. BioRxiv.
1149 Jones, D.T. (1999). Protein secondary structure prediction based on position-specific scoring
1150 matrices. Journal of Molecular Biology *292*, 195-202.
1151 Kazmierczak, B.I., Lebron, M.B., and Murray, T.S. (2006). Analysis of FimX, a
1152 phosphodiesterase that governs twitching motility in *Pseudomonas aeruginosa*. Mol
1153 Microbiol *60*, 1026-1043.
1154 Kloosterman, A.M., Shelton, K.E., van Wezel, G.P., Medema, M.H., and Mitchell, D.A. (2020).
1155 RRE-Finder: a Genome-Mining Tool for Class-Independent RiPP Discovery. mSystems *5*,
1156 e00267-00220.
1157 Kourelis, J., and van der Hoorn, R.A.L. (2018). Defended to the Nines: 25 Years of Resistance
1158 Gene Cloning Identifies Nine Mechanisms for R Protein Function. Plant Cell *30*, 285-299.
1159 Krivak, R., and Hoksza, D. (2018). P2Rank: machine learning based tool for rapid and
1160 accurate prediction of ligand binding sites from protein structure. J Cheminform *10*, 39.
1161 Laemmli, U.K. (1970). Cleavage of structural proteins during the assembly of the head of
1162 bacteriophage T4. Nature *227*, 680-685.
1163 Lapin, D., Bhandari, D.D., and Parker, J.E. (2020). Origins and Immunity Networking
1164 Functions of EDS1 Family Proteins. Annu Rev Phytopathol *58*, 253-276.
1165 Leavitt, A., Yirmiya, E., Amitai, G., Lu, A., Garb, J., Morehouse, B.R., Hobbs, S.J., Kranzusch,
1166 P.J., and Sorek, R. (2022). Viruses inhibit TIR gcADPR signaling to overcome bacterial
1167 defense. BioRxiv.
1168 Lee, H.C., and Zhao, Y.J. (2019). Resolving the topological enigma in Ca(2+) signaling by cyclic
1169 ADP-ribose and NAADP. J Biol Chem *294*, 19831-19843.

1170 Lenth, R.V. (2022). emmeans: Estimated Marginal Means, aka Least-Squares Means. R
1171 package version 1.7.3.
1172 Levy, A., Salas Gonzalez, I., Mittelviefhaus, M., Clingenpeel, S., Herrera Paredes, S., Miao, J.,
1173 Wang, K., Devescovi, G., Stillman, K., Monteiro, F.*, et al.* (2018). Genomic features of
1174 bacterial adaptation to plants. Nat Genet *50*, 138-150.
1175 Li, W., Chiang, Y.H., and Coaker, G. (2013). The HopQ1 effector's nucleoside hydrolase-like
1176 domain is required for bacterial virulence in arabidopsis and tomato, but not host
1177 recognition in tobacco. PLoS One *8*, e59684.
1178 Liu, Q., Kriksunov, I.A., Graeff, R., Lee, H.C., and Hao, Q. (2007). Structural basis for
1179 formation and hydrolysis of the calcium messenger cyclic ADP-ribose by human CD38. J Biol
1180 Chem *282*, 5853-5861.
1181 Lo, T., Koulena, N., Seto, D., Guttman, D.S., and Desveaux, D. (2017). The HopF family of
1182 *Pseudomonas syringae* type III secreted effectors. Mol Plant Pathol *18*, 457-468.
1183 Ma, S., Lapin, D., Liu, L., Sun, Y., Song, W., Zhang, X., Logemann, E., Yu, D., Wang, J.,
1184 Jirschitzka, J.*, et al.* (2020). NAD+ cleavage activity by animal and plant TIR domains in cell
1185 death pathways. Science *370*.
1186 Manik, M.K., Shi, Y., Li, S., Zaydman, M.A., Damaraju, N., Eastman, S., Smith, T.G., Gu, W.,
1187 Masic, V., Mosaiab, T.*, et al.* (2022). Chemical structures of cyclic ADP ribose (cADPR)
1188 isomers and the molecular basis of their production and signaling. BioRxiv.
1189 Menetrey, J., Flatau, G., Boquet, P., Menez, A., and Stura, E.A. (2008). Structural basis for
1190 the NAD-hydrolysis mechanism and the ARTT-loop plasticity of C3 exoenzymes. Protein Sci
1191 *17*, 878-886.
1192 Minh, B.Q., Schmidt, H.A., Chernomor, O., Schrempf, D., Woodhams, M.D., von Haeseler, A.,
1193 and Lanfear, R. (2020). IQ-TREE 2: New Models and Efficient Methods for Phylogenetic
1194 Inference in the Genomic Era. Mol Biol Evol *37*, 1530-1534.
1195 Mirdita, M., Schütze, K., Moriwaki, Y., Heo, L., Ovchinnikov, S., and Steinegger, M. (2022).
1196 ColabFold - Making protein folding accessible to all. BioRxiv.
1197 Munshi, C., Aarhus, R., Graeff, R., Walseth, T.F., Levitt, D., and Lee, H.C. (2000). Identification
1198 of the enzymatic active site of CD38 by site-directed mutagenesis. J Biol Chem *275*, 21566-
1199 21571.
1200 O'Boyle, N., Banck, M., James, C., Morley, C., Vandermeersch, T., and Hutchison, G. (2011).
1201 Open Babel: An open chemical toolbox. Journal of Cheminformatics *3*.
1202 Ofir, G., Herbst, E., Baroz, M., Cohen, D., Millman, A., Doron, S., Tal, N., Malheiro, D.B.A.,
1203 Malitsky, S., Amitai, G.*, et al.* (2021). Antiviral activity of bacterial TIR domains via immune
1204 signalling molecules. Nature *600*, 116-120.
1205 Pandit, S.B., and Skolnick, J. (2008). Fr-TM-align: a new protein structural alignment method
1206 based on fragment alignments and the TM-score. BMC Bioinformatics *9*, 531.
1207 Paradis, E., and Schliep, K. (2019). ape 5.0: an environment for modern phylogenetics and
1208 evolutionary analyses in R. Bioinformatics *35*, 526-528.
1209 Parks, D.H., Imelfort, M., Skennerton, C.T., Hugenholtz, P., and Tyson, G.W. (2015). CheckM:
1210 assessing the quality of microbial genomes recovered from isolates, single cells, and
1211 metagenomes. Genome Res *25*, 1043-1055.
1212 Pereira, J., and Alva, V. (2021). How do I get the most out of my protein sequence using
1213 bioinformatics tools? Acta Crystallogr D Struct Biol *77*, 1116-1126.
1214 Petersen, C., and Moller, L.B. (2001). The RihA, RihB, and RihC ribonucleoside hydrolases of
1215 *Escherichia coli.* Substrate specificity, gene expression, and regulation. J Biol Chem *276*, 884-
1216 894.

1217 Petnicki-Ocwieja, T., Schneider, D.J., Tam, V.C., Chancey, S.T., Shan, L., Jamir, Y., Schechter,
1218 L.M., Janes, M.D., Buell, C.R., Tang, X.*, et al.* (2002). Genomewide identification of proteins
1219 secreted by the Hrp type III protein secretion system of *Pseudomonas syringae* pv. *tomato*
1220 DC3000. Proc Natl Acad Sci U S A *99*, 7652-7657.
1221 R.Core.Team (2020). R: A language and environment for statistical computing. (Vienna,
1222 Austria: R Foundation for Statistical Computing,).
1223 Ramakrishnan, L., Muller-Steffner, H., Bosc, C., Vacquier, V.D., Schuber, F., Moutin, M.J.,
1224 Dale, L., and Patel, S. (2010). A single residue in a novel ADP-ribosyl cyclase controls
1225 production of the calcium-mobilizing messengers cyclic ADP-ribose and nicotinic acid
1226 adenine dinucleotide phosphate. J Biol Chem *285*, 19900-19909.
1227 Salentin, S., Schreiber, S., Haupt, V.J., Adasme, M.F., and Schroeder, M. (2015). PLIP: fully
1228 automated protein-ligand interaction profiler. Nucleic Acids Res *43*, W443-447.
1229 Sanders, B.D., Jackson, B., and Marmorstein, R. (2010). Structural basis for sirtuin function:
1230 what we know and what we don't. Biochim Biophys Acta *1804*, 1604-1616.
1231 Schliep, K.P. (2011). phangorn: phylogenetic analysis in R. Bioinformatics *27*, 592-593.
1232 Schreiber, K.J., Chau-Ly, I.J., and Lewis, J.D. (2021). What the Wild Things Do: Mechanisms of
1233 Plant Host Manipulation by Bacterial Type III-Secreted Effector Proteins. Microorganisms *9*.
1234 Seemann, T. (2014). Prokka: rapid prokaryotic genome annotation. Bioinformatics *30*, 2068-
1235 2069.
1236 Shi, Y., Kerry, P.S., Nanson, J.D., Bosanac, T., Sasaki, Y., Krauss, R., Saikot, F.K., Adams, S.E.,
1237 Mosaiab, T., Masic, V.*, et al.* (2022). Structural basis of SARM1 activation, substrate
1238 recognition, and inhibition by small molecules. Mol Cell.
1239 Soding, J., Biegert, A., and Lupas, A.N. (2005). The HHpred interactive server for protein
1240 homology detection and structure prediction. Nucleic Acids Res *33*, W244-248.
1241 Srouji, J.R., Xu, A., Park, A., Kirsch, J.F., and Brenner, S.E. (2017). The evolution of function
1242 within the Nudix homology clan. Proteins *85*, 775-811.
1243 Stivala, A., Wybrow, M., Wirth, A., Whisstock, J.C., and Stuckey, P.J. (2011). Automatic
1244 generation of protein structure cartoons with Pro-origami. Bioinformatics *27*, 3315-3316.
1245 Sun, Y., Li, P., Shen, D., Wei, Q., He, J., and Lu, Y. (2019). The *Ralstonia solanacearum*
1246 effector RipN suppresses plant PAMP-triggered immunity, localizes to the endoplasmic
1247 reticulum and nucleus, and alters the NADH/NAD(+) ratio in *Arabidopsis*. Mol Plant Pathol
1248 *20*, 533-546.
1249 Takamura-Enya, T., Watanabe, M., Totsuka, Y., Kanazawa, T., Matsushima-Hibiya, Y.,
1250 Koyama, K., Sugimura, T., and Wakabayashi, K. (2001). Mono(ADP-ribosyl)ation of 2'-
1251 deoxyguanosine residue in DNA by an apoptosis-inducing protein, pierisin-1, from cabbage
1252 butterfly. Proc Natl Acad Sci U S A *98*, 12414-12419.
1253 Thompson, J., Higgins, D., and Gibson, T. (1994). CLUSTAL W: improving the sensitivity of
1254 progressive multiple sequence alignment through sequence weighting, position-specific gap
1255 penalties and weight matrix choice. Nucleic Acids Res *22*, 4673-4680.
1256 Tohgo, A., Munakata, H., Takasawa, S., Nata, K., Akiyama, T., Hayashi, N., and Okamoto, H.
1257 (1997). Lysine 129 of CD38 (ADP-ribosyl cyclase/cyclic ADP-ribose hydrolase) participates in
1258 the binding of ATP to inhibit the cyclic ADP-ribose hydrolase. J Biol Chem *272*, 3879-3882.
1259 Toshchakov, V.Y., and Neuwald, A.F. (2020). A survey of TIR domain sequence and structure
1260 divergence. Immunogenetics *72*, 181-203.
1261 Turko, I.V., Francis, S.H., and Corbin, J.D. (1998). Potential roles of conserved amino acids in
1262 the catalytic domain of the cGMP-binding cGMP-specific phosphodiesterase. J Biol Chem
1263 *273*, 6460-6466.

1264 Ve, T., Williams, S.J., and Kobe, B. (2015). Structure and function of Toll/interleukin-1
1265 receptor/resistance protein (TIR) domains. Apoptosis *20*, 250-261.
1266 Vinatzer, B.A., Jelenska, J., and Greenberg, J.T. (2005). Bioinformatics Correctly Identifies
1267 Many Type III Secretion Substrates in the Plant Pathogen *Pseudomonas syringae* and the
1268 Biocontrol Isolate *P. fluorescens* SBW25. MPMI *18*, 877-888.
1269 Wan, L., Essuman, K., Anderson, R.G., Sasaki, Y., Monteiro, F., Chung, E.H., Osborne
1270 Nishimura, E., DiAntonio, A., Milbrandt, J., Dangl, J.L*., et al.* (2019). TIR domains of plant
1271 immune receptors are NAD(+)-cleaving enzymes that promote cell death. Science *365*, 799-
1272 803.
1273 Ward, J.L., Forcat, S., Beckmann, M., Bennett, M., Miller, S.J., Baker, J.M., Hawkins, N.D.,
1274 Vermeer, C.P., Lu, C., Lin, W*., et al.* (2010). The metabolic transition during disease following
1275 infection of *Arabidopsis thaliana* by *Pseudomonas syringae* pv. *tomato*. Plant J *63*, 443-457.
1276 Wei, H.L., Chakravarthy, S., Mathieu, J., Helmann, T.C., Stodghill, P., Swingle, B., Martin,
1277 G.B., and Collmer, A. (2015). *Pseudomonas syringae* pv. *tomato* DC3000 Type III Secretion
1278 Effector Polymutants Reveal an Interplay between HopAD1 and AvrPtoB. Cell Host Microbe
1279 *17*, 752-762.
1280 Wickham, H. (2007). Reshaping Data with the reshape Package. Journal of Statistical
1281 Software *21*, 1-20.
1282 Wickham, H. (2016). ggplot2: Elegant Graphics for Data Analysis (New York: Springer-Verlag
1283 ).
1284 Wolters, V., Rosche, A., Bauche, A., Kulow, F., Harneit, A., Fliegert, R., and Guse, A.H. (2019).
1285 NAD binding by human CD38 analyzed by Trp189 fluorescence. Biochim Biophys Acta Mol
1286 Cell Res *1866*, 1189-1196.
1287 Xin, X.F., Kvitko, B., and He, S.Y. (2018). *Pseudomonas syringae:* what it takes to be a
1288 pathogen. Nat Rev Microbiol *16*, 316-328.
1289 Young, J.M. (2010). Taxonomy of *Pseudomonas syringae*. Journal of Plant Pathology *92*,
1290 S1.5-S1.14.
1291 Yu, D., Song, W., Tan, E.Y.J., Liu, L., Cao, Y., Jirschitzka, J., Li, E., Logemann, E., Xu, C., Huang,
1292 S*., et al.* (2022). TIR domains of plant immune receptors are 2',3'-cAMP/cGMP synthetases
1293 mediating cell death. Cell.
1294 Yuan, H., and Marmorstein, R. (2012). Structural basis for sirtuin activity and inhibition. J Biol
1295 Chem *287*, 42428-42435.
1296 Yuan, J., and He, S.Y. (1996). The *Pseudomonas syringae* Hrp Regulation and Secretion
1297 System Controls the Production and Secretion of Multiple Extracellular Proteins. J Bacteriol
1298 *178*, 6399-6402.
1299 Zhou, H., Morgan, R.M., Guttman, S., and Ma, W. (2009). Allelic Variants of the
1300 *Pseudomonas syringae* Type III Effector HopZ1 Are Differentially Recognized by Plant
1301 Resistance Systems. MPMI *22*, 176-189.
1302